

# Cohesive zone modeling of the buckling behavior of a fusion-joined, additive-manufactured wind blade

Dongyang Cao<sup>1,\*</sup>, Hongbing Lu<sup>1</sup>, Daniel Todd Griffith<sup>1</sup>

Academic Editor: Raul D.S.G. Campilho

#### **Abstract**

In this article, the use of additive-manufactured thermoplastics, specifically polylactic acid (PLA), to fabricate segments of wind turbine blades with core sandwich composites was verified through their compressive bucking performance, demonstrating their cost-effectiveness in manufacturing and transportation. A small wind blade was constructed by joining these segments to demonstrate their application potential in renewable energy technologies. The study's focus was on the compressive buckling behavior of these fusion-joined blades, particularly on the heterogeneity at the resistance welding bond line. An approach was adopted to integrate a hybrid of solid and cohesive elements within the cohesive zone modeling (CZM) framework using the Abaqus−Riks method. This allowed us to insert a thin layer of solid−cohesive elements at the bond line, enhancing the fidelity of our simulations. The validity of our numerical results was examined by comparing them with the surface strain field measured by digital image correlation (DIC) and assessing the compressive response. Furthermore, the applicability of classical Euler and Johnson formulas was evaluated in predicting buckling loads and modes. The Euler formula was found adequate for the first flexural buckling mode in beams with high slenderness ratios (≥12). Our findings demonstrate that the hybrid CZM approach effectively models the buckling behavior of fusion-joined beams, accommodating a range of slenderness ratios (6 to 18) and various buckling modes. This study provides insights into the structural analysis of fusion-joined components for potential applications of additive manufacturing in wind energy.

**Keywords:** cohesive zone modeling, green manufacturing, sustainability, thin-walled lattice structure, fusion joining, material extrusion

**Citation:** Cao D, Lu H, Griffith DT. Cohesive zone modeling of the buckling behavior of a fusion-joined, additive-manufactured wind blade. *Academia Materials Science* 2024;1. https://doi.org/10.20935/AcadMatSci7281

#### 1. Introduction

Large-scale wind turbines are pivotal in the utility-scale renewable energy sector due to their high power output, efficiency, and minimal emission of greenhouse gases and other environmental pollutants [1-3]. Conversely, small-scale wind turbines have garnered a significant interest for individual use in rural areas [4]. Now capable of producing kilowatt-level power, these turbines offer promising alternatives for localized energy generation. Notable examples include the model MG4520 wind turbine, which, with its 2.1-m rotor diameter, was found by Freere et al. to produce a power output of 0.3 kW [5]. Similarly, Hirahara et al. tested the model NACA 2404 wind turbine (r = 0.5 m) and found it achieves a maximum power output of 0.2 kW under a 20 m/s wind speed [6]. Additionally, Matsumiya et al. designed and tested the model SD7307 wind turbine (r = 1.8 m), demonstrating a 1 kW power output under a 50 m/s wind speed, even without a pitch control system [7].

According to a report from the US Department of Energy [8], a 1.5 kW wind turbine operating at an average annual wind speed of 6.26 m/s could sufficiently meet the power requirements of a typical home (300 kWh/month). Hence, small-scale wind

turbines offer a viable solution for electricity supply in areas beyond the power grid.

In addition to their role in power generation, small-scale wind turbines are often utilized as scaled-down models for testing large-scale wind turbines [9]. This makes it crucial to accurately assess the performance of a downscaled small-scale wind turbine to evaluate the power output and structural integrity of its larger counterpart, which can take several months or even years to install, owing to the complexities of transportation and installation [10].

Presently, routine maintenance for wind turbine blades includes surface coating, sealing, resin injection, and various repair methods such as plug, patch, and scarf repairs [11]. Wind turbine blade repair is notably costly. Stephenson reported that maintenance expenses can amount to 20–25% of the levelized cost of energy (LCOE) over a turbine's lifespan [12]. A significant factor contributing to these high costs is the lengthy repair time required for adhesive bonding, which can exceed 24 h.

Resistance welding with metal meshes offers a much quicker repair time, in a matter of just a few minutes (3–5 min), aligning

\*email: dxc172430@utdallas.edu

<sup>&</sup>lt;sup>1</sup>Department of Mechanical Engineering, The University of Texas at Dallas, Richardson, TX 75080, USA.

well with UV light photocuring processes [13]. This rapid repair method could substantially reduce maintenance costs. However, ensuring that the structural performance of the repaired blade matches that of the original blade remains a subject for further investigation.

3D printing emerges as an exceptionally suitable manufacturing method for small-scale wind turbines, offering advantages such as low cost, reduced carbon emissions, rapid prototyping, and the ability to create complex architectures, which are not as easily achieved with conventional manufacturing techniques [4, 14, 15]. The process encompasses various techniques, including fused deposition modeling (FDM), powder—liquid 3D printing, stereo-lithography, selective laser sintering, and 3D plotting [14, 16]. Among these, FDM is particularly noteworthy for its cost-effectiveness and relatively high strength-to-weight ratio [14, 15, 17]. This ratio can be further optimized by adjusting layer height, infill pattern, and infill density in the STL file.

Furthermore, using materials with a high strength-to-weight ratio could significantly broaden the potential applications of small-scale wind turbines [18]. This aspect in 3D printing enhances the durability and efficiency of wind turbines and aligns well with the overarching goals of sustainable and innovative energy solutions.

FDM is a popular method for printing small wind turbine blades and prototypes. While FDM offers several advantages over traditional manufacturing techniques, it also faces certain limitations, notably in build size, which is constrained by the machine's volume. Li et al. and Duty et al. have highlighted this limitation, noting that the build volume of a typical FDM 3D printer is generally less than  $80 \times 80 \times 80$  cm³ [19, 20].

However, advancements in this field have been significant. For instance, Duty et al. reported that Ingersoll Machine Tools and Oak Ridge National Laboratory developed one of the world's largest 3D printers, capable of a build volume of  $6\times2.4\times1.8~\text{m}^3$  and operating at a printing speed of 80 lb/h [20]. Despite this technological advancement, such large-scale 3D printers are not widely available, leaving most users with access only to smaller, commercial FDM printers.

Commercial 3D printers often face size limitations, making it challenging to print small-scale blades (0.5–2 m) in one piece. To overcome this barrier, these blades can be printed in segments and subsequently joined together. The traditional method of mechanical fastening is not ideal for 3D-printed structures due to several drawbacks: it adds extra weight, creates stress concentrations at metallic joints, risks structural delamination from drilling holes, and requires intensive labor [21–23]. An alternative method is the fusion joining process, which involves hotmelting segmented regions of the thermoplastic structure. This technique is advantageous because it is cost-effective, eliminates the need for surface preparation, and ensures good bonding quality [24]. Common filament materials used in 3D printing, such as acrylonitrile butadiene styrene and PLA, are thermoplastics, making them suitable for high-temperature joining.

The fusion joining process for thermoplastic-matrix wind turbine blades primarily involves techniques, such as ultrasonic, induction, and resistance welding [25, 26]. Among these, resistance welding is particularly noteworthy. This process uses a current to heat an electrically conductive element (e.g., carbon fiber or metal mesh) to a temperature above the glass transition point of

thermoplastic matrix. During this process, the material is sandwiched between the polymer matrix, and pressure is applied to ensure good bonding. The heat generation in resistance welding follows Joule's law, with the energy dissipation proportional to the wire resistance, current level, and welding time [27]. Advantages of resistance welding include low labor costs, reduced labor hours, and a simple heat generation rule that can be easily understood through analytical approaches [25].

Previous reports on resistance-welded nonbiodegradable thermoplastic composites—including combinations, such as thermoplastic composites with graphite [28], carbon [29-31], and glass fiber [32], alongside materials like polyethylene (PE), polypropylene (PP), polyetherimide (PEI), polyphenylene sulfide (PPS), polyetheretherketone (PEEK), and Elium® 188 [25], and heating elements, such as UD carbon prepreg, carbon fabric, stainless steel mesh, carbon nanotube (CNT)-polymer film, and PP polymer film—have shown that factors like the parameters of resistance welding and the type of heating element can significantly influence bonding quality [26, 27, 33, 34]. In this study, we use resistance welding with a metal mesh to fusion join the segments of a wind turbine blade. To our knowledge, the bonding quality between the metal mesh and 3D-printed parts has not been comprehensively explored before, and this paper aims to address this gap.

In this study, the role of bond line quality on compressive buckling behavior was explored, employing both experimental and simulation approaches. Experiments involving compressive buckling were conducted on a fusion-joined wind turbine blade. Concurrently, analytical work was carried out using finite element methods and classical buckling theories. In previous studies, using solid or cohesive elements in the bonding line of models led to inaccuracies in simulating the lateral displacement of fusion-joined beams [35, 36]. Cohesive elements, being much softer than solid elements, require careful adjustment in their ratio to solid elements. This adjustment helps maintain a minor variation in strength and aligns lateral displacement between the model and the actual experiments.

CZM has gained popularity for analyzing the mechanical properties of fiber-reinforced composites, addressing issues like delamination, crack initiation, and material softening, mainly focusing on the interphase debonding mechanism [37–40]. However, the suitability of the CZM approach for fusion-joined thin-wall lattice structures remains unclear, especially concerning both linear and nonlinear compressive buckling performance.

This study also explored the role of resistance welding and adhesive bonding processes on the compressive buckling behavior of small-scale wind turbine blades, explicitly focusing on fusion-joined 3D-printed 14-inch beam samples. A detailed characterization of the bonding performance using compressive buckling tests and finite element modeling (FEM) was utilized in this study. For this purpose, multiple 7-inch chord blades were designed and fabricated using the FDM process. These blades were then fusion joined using resistance welding and epoxy adhesive techniques. The buckling mode and critical buckling load were determined through compressive buckling tests, complemented by analytical approaches based on Euler and Johnson theories. Ultimately, hybrid element CZMs were developed to accurately define the critical buckling loads and buckling modes for various types of 14-inch beams.

#### 2. Materials and methods

This section outlines the procedures for preparing the 3D-printed samples and provides detailed descriptions of the experimental methodologies employed in this study.

#### 2.1. Materials

For the 3D printing of our samples, we used PLA filaments from Craftbot (Carrollton, TX, USA), each with a diameter of 1.75 mm. PLA is chosen for its high strength-to-weight ratio and its ability to be printed at lower temperatures than other 3D printing materials [41, 42]. Each filament spool used in the process weighed 1 kg. To facilitate the fusion joining of the two 7-inch segments into a 14-inch beam, Ni-Cu metal alloy meshes were sourced from McMaster-Carr (Elmhurst, IL, USA). The chosen mesh specifications included an opening size of 0.07 mm, an open area of 34%, and a wire diameter of 50 µm [43]. This opening size was specifically selected to ensure effective impregnation of the resin into the mesh, while the small wire diameter was aimed at enhancing heating efficiency. Plexus MA310 highstrength MMA adhesives from Perigee Direct (North Richland Hills, TX, USA), were also used as bonding agents. This adhesive is frequently used to manufacture wind turbine blades, particularly for joining segments in thermoplastic polymer matrix structures [25].

#### 2.2. Sample preparations

The FDM process and infill patterns utilized in our study are illustrated in **Figures 1** and **2** of our previous work [44]. For printing the 7-inch chords, a Craftbot 3 FDM dual-extrusion 3D printer from Craftbot (Carrollton, TX, USA), was employed. This printer features a total build volume of 250 × 200 × 200 mm³, a printing temperature range of 20–300°C, and a maximum printing speed of 200 mm/s [43]. The chord geometries were designed using AutoCAD (Autodesk, San Francisco, CA, USA) or SolidWorks software (Dassault Systemes, Waltham, MA, USA) and exported as STL files. These files were imported into CraftWare PRO software (Craftbot, Carrollton, TX, USA).

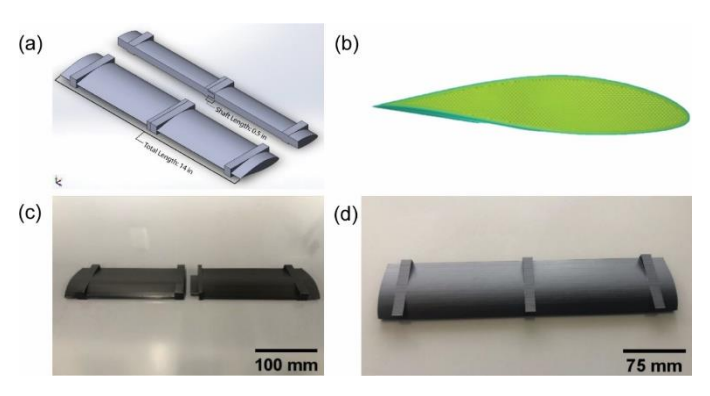


**Figure 1 •** Schematic and actual samples of the 3D-printed 7-inch chords. (a) Isometric view of the segmented 7-inch chord featuring a narrow gap. (b) Cross-sectional view showing the internal topology of the segmented 7-inch chord. (c) Actual 3D-printed segmented 7-inch chord with a narrow opening. (d) Fully 3D-printed single-piece 14-inch beam.

Various 3D print settings were properly modified, including printing speed, travel speed, nozzle diameter, layer height, nozzle and bed temperatures, and infill density. The printing speed was set to 60 mm/s, with a travel speed of 120 mm/s. A 0.25 mm

diameter stainless steel nozzle and a layer height of 0.2 mm were used to ensure a smooth surface finish on the samples. The nozzle temperature was maintained at 215°C and the bed temperature at 60°C. An infill density of 40% was chosen, with the infill pattern oriented at  $+45^{\circ}/-45^{\circ}$  angles. Before each 3D printing job, the nozzle-to-bed level was calibrated, and both the nozzle and bed were preheated to prevent nozzle clogging.

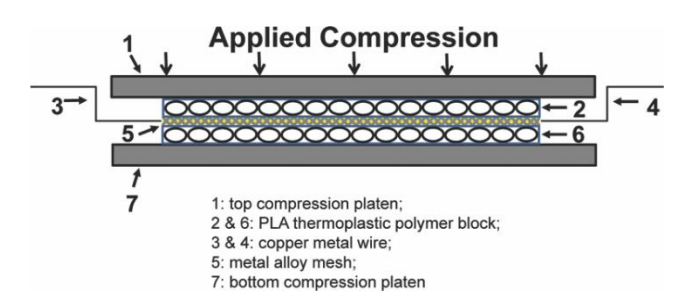


**Figure 2** • Schematic diagram of the resistance welding setup. Key components are labeled as follows: (1) and (7) represent the compression platens; (2) and (6) are the thermoplastic polymer blocks; (3) and (4) denote the thin metallic wires; and (5) is the metallic mesh used in the process.

#### 2.3. Design of the 7-inch chord

The SNL-100-03 wind turbine blade was used as the prototype for our 7-inch chord, a design that has been extensively utilized and referenced in previous publications [45]. This prototype is known for its high strength-to-weight ratio and cost-effectiveness, featuring an optimized skin-core material, shear web, spar cap, and blade geometry, especially compared to an all-glass-based design [46–48]. To ensure structural stability and avoid critical loading regions, a segmented section of the blade geometry from 76.4% of the total blade length, starting from the root, was selected [49, 50]. Additionally, a properly designed shaft was incorporated to enhance the bonding quality [51].

This blade geometry and shaft were downscaled to a 7-inch chord for mechanical characterization. Three variations of this 14-inch chord were properly designed: a single piece (with no segmentation), segmented with a narrow gap (gap = 0.10 mm), and segmented with a rectangular flat. The gap in the narrow gap design, intended for adhesive bonding, represents the distance between the shaft and the socket. The rectangular segmentation design was explicitly for resistance welding, while the single-piece 14-inch beam served as a benchmark for comparison. Figure 1a and 1b illustrates the wind turbine blade design, whereas Figure 1c and 1d depicts the 3D-printed 14-inch beams created by fusion joining two 7-inch chords. A detailed description of the shaft and socket was provided in the previous publication.

#### 2.4. Resistance welding

**Figure 2** shows a schematic of our resistance welding setup. A detailed description of the resistance welding process and its procedures is provided in the subsequent paragraphs.

Initially, the designated resistance welding areas (13.97  $\times$  76.20 mm²) of the 3D-printed parts were meticulously cleaned using 75% ethanol. This step was crucial to remove any contaminants and ensure better bonding quality. Subsequently, a Ni–Cu metal alloy mesh was positioned between the 3D-printed segments. Two thin copper wires, each measuring 90 mm in length to

maintain consistent wire resistance, were connected to the mesh to facilitate electrical conductivity.

A model 5969 Instron universal testing system (Instron, Norwood, MA, USA) along with compression platens was applied for applying uniform pressure and controlled displacement during the welding process. Heating was provided using a model 9202 multirange programmable DC power supply (B&K Precision, Yorba Linda, CA, USA), capable of maximum outputs of 60 V, 15 A, and 360 W, respectively [52].

At the onset of the process, an initial pressure of 290.08 psi was applied to the Ni–Cu metal alloy mesh. As the polymer in the bonding region began to melt, this pressure was reduced to slow the displacement rate. The displacement rate was set as 0.6 mm/min, with a total travel distance of 3 mm. The power settings were adjusted to 1.5 V, 1.7 V, 1.9 V, 2.1 V, and 2.3 V for resistance welding times of 30 s, 30 s, 30 s, 90 s, and 30 s, respectively, with a current limit of 15 A. A ramp heating set was programmed to avoid the application of a high current pulse and to ensure a steady and uniform heat distribution across the metal mesh.

#### 2.5. Uniaxial compressive buckling tests

Our study focused on the critical buckling load, critical lateral displacement, and energy absorption characteristics of four different types of 14-inch beams. For each beam type, three tests were conducted. The effective length of the samples was 101.6 mm, corresponding to a slenderness ratio of 6. All samples were subjected to fixed boundary conditions at both ends. The tests were performed at a crosshead speed of 1.5 mm/min, following ASTM D6641 standards [53].

During the uniaxial compressive buckling tests, a Nikon D7100 camera (Nikon, Melville, NY, USA) was used, equipped with a 24-mm lens and capable of capturing images at a resolution of 3,840  $\times$  2,748 pixels, to capture the buckling mode of the samples. This camera setup allowed us to acquire images every second. Positioned at a distance of 1.3 m, it was ideal for capturing the entire effective gauge length of the samples within the region of interest. A Nila Varsa LED light was used during the imaging process to ensure proper illumination. Furthermore, the equation for calculating energy absorption in these tests is as follows:

$$U = \int_{0}^{v_{\text{max}}} F du \tag{1}$$

where U is the total energy absorption, calculated based on the area enclosed by the compressive load-displacement curve, in this context, u represents the compressive displacement,  $v_{\max}$  is the maximum compressive displacement observed until a fracture occurs, and F refers to the uniaxial compressive load. Therefore, the energy absorption U is essentially the integral of the load-displacement curve up to the point of maximum displacement or fracture.

### 2.6. Euler and Johnson buckling under two clamped ends condition

According to the theory of elastic stability [54], it is possible to determine the critical local, buckling load, and lateral displacement of the 14-inch beam. **Figure 3** illustrates the boundary condition of the 7-inch chord when subjected to compressive load.

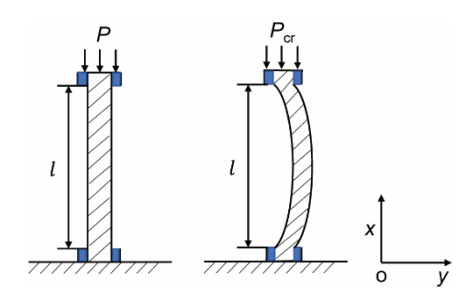


**Figure 3** • Schematic of the boundary condition of the compressive buckling tests.

The Euler buckling load is calculated by:

$$P_{\rm cr} = \frac{4n^2\pi^2 EI}{l^2} (n = 1, 2, 3...)$$
 (2)

where E is Young's modulus of the PLA, I is the moment of inertia of the cross section, and l is the length of the rectangular beam.

The lateral displacement is given by:

$$y = B\left(\cos\left(\frac{2n\pi d}{l}\right) - 1\right) (n = 1, 2, 3...)$$
(3)

where y is the lateral deflection, B is the magnitude of the deflection, d is the position of interest in the longitudinal direction, and l is the effective length of the beam.

The critical compressive buckling load under fixed ends is calculated using the Johnson parabola formula [54]:

$$P_{\rm cr} = A \left( \sigma_y - \frac{1}{E} \left( \frac{\sigma_y}{2n\pi} \right)^2 \left( 0.5l \sqrt{\frac{A}{I}} \right)^2 \right) (n = 1, 2, 3...)$$
(4)

where A and  $\sigma_y$  are the cross-sectional area and yield stress of the beam, respectively. I is the second moment of inertia of the cross section of the beam.

#### 2.7. Finite element model

To simulate the various buckling modes and post-buckling behavior of the segmented 14-inch beam, a finite element model featuring a CZM bonding region was established. The Riks model was employed to analyze post-buckling behavior. The design of the 14-inch beam included a lattice truss infill, and the outer shell had a thickness of 0.8 mm. **Figure 4** displays the topology of the lattice truss. The parameters defining the triangular pyramid within this structure are side length a = 5.85 mm, angle  $a = 34.9^{\circ}$ , and height b = 4.78 mm.

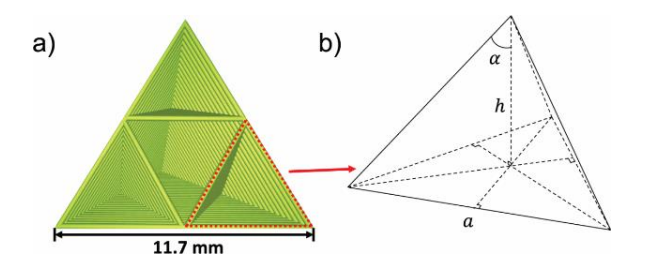


**Figure 4 •** FEM of a unit cell, illustrating the infill patterns in the 3D-printed 14-inch beam. (a) Lattice truss infill of the FDM-printed 14-inch beam, as generated from AutoCAD software. (b) Detailed view of the unit triangular pyramid structure.

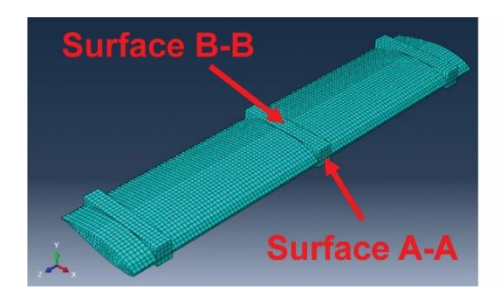
**Figure 5** shows the 3D CZM complete with meshing. Finer meshes were employed, specifically in the fusion-joined region of the 14-inch beam, to ensure a precise solution. A detailed explanation of the CZM is provided in the subsequent paragraph.

In this model, linear hexahedral elements of type C3D8R were employed. To ensure fast convergence and avoid mesh-dependent results, the total number of elements used was 13,580. The entire 14-inch beam was modeled as a linearly elastic solid, with plasticity also incorporated to represent buckling and post-buckling modes accurately following plastic deformation.

The model considered multiple slenderness ratios for the 14-inch beam, specifically 6, 12, and 18, to assess the effect of geometry

on buckling performance. Notably, a slenderness ratio of 18 corresponds to the realistic numerical value for the model SNL-100-03 [45]. Moreover, the model includes two buckling modes for the adhesive-bonded segmented 14-inch beam, with the buckling mode of the single-piece-type serving as a benchmark.

The lateral displacement, critical buckling loads, and energy absorption for these two types of 14-inch beams will be detailed in the Results and Discussion section. The mechanical properties of the 3D-printed 14-inch beams are as follows: Young's modulus E=3.5 GPa, shear modulus G=1.4 GPa, and Poisson's ratio v=0.3. The mechanical properties and cohesive parameters of each type of 14-inch beam are listed in **Tables 1** and **2**.



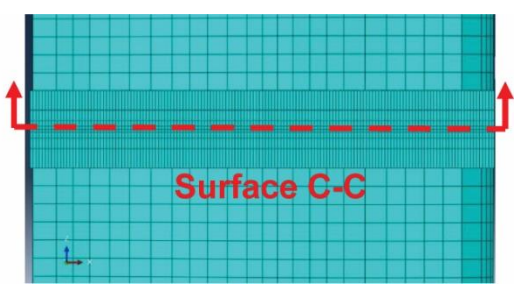


**Figure 5** • Schematic representation of the FEM model incorporating CZM in the bonding regions. This model depicts a beam assembled by connecting three distinct types of 14-inch beams, specifically analyzed under conditions of compressive buckling. Surfaces A-A, B-B, and C-C indicate side face, top face, and bonding interface of the middle rectangular block, respectively.

**Table 1 •** Mechanical properties and cohesive parameters on the bonding region of each type of 14-inch beam in the hybrid element CZM approach

Sample (14-inch beam)	E <sub>solid</sub> (GPa)	E <sub>nn</sub> (MPa/mm)	E <sub>ss</sub> (MPa/mm)	E <sub>tt</sub> (MPa/mm)	V <sub>solid</sub> (%)	V <sub>cohesive</sub> (%)	t (mm)
Adhesive bonded	1.12	1	1	1	23	77	0.01
Resistance welded	3.75	2.5	2.5	2.5	20	80	0.25

Note: In the notation, "solid" and "cohesive" refer to the solid and cohesive elements in the bonding region, respectively. The notations "nn", "ss", and "tt" represent the longitudinal, transverse, and normal directions within the cohesive zone, respectively. Additionally, "t" denotes the thickness of the adhesive layer.

Table 2 • Cohesive parameters on the bonding region of each type of 14-inch beam of the CZM approach

Sample (14-inch beam)	E <sub>nn</sub> (GPa/mm)	E <sub>ss</sub> (GPa/mm)	E <sub>tt</sub> (GPa/mm)	t (mm)
Resistance welded	1.83	1.83	1.83	10-4
Adhesive bonded	1.12	1.12	1.12	10-4

In the models of both the adhesive-bonded and resistance-welded segmented 14-inch beams, a hybrid element approach using CZM was employed. This involved the insertion of an infinitesimally thin cohesive layer—10  $\mu m$  for adhesive bonded and 25  $\mu m$  for resistance welding—comprised of solid and cohesive elements between the two segmented regions. This layer was designed to capture the interfacial bonding on the post-buckling performance of the beams accurately. For the adhesive-bonded region, a bilinear traction—separation law was applied.

Furthermore, the 3D cohesive stiffness in these regions was assumed to be uniform [55]. Additionally, a viscous regulation was incorporated into the interphase region to stabilize the computational solution and prevent a sudden loss of stiffness.

#### 3. Results and discussion

## 3.1. Mechanical characterization of the 14-inch beam in compression

**Figure 6** displays the relationship between compressive load and compressive displacement for the three different types of 14-inch beams. All three variations demonstrate a ductile failure mode, indicating robust resistance to catastrophic failure. Notably, the single, slender 14-inch beam produced via 3D printing exhibits the highest compressive load capacity.

The investigation revealed that adhesive bonding, while effective, shows a somewhat lower stiffness compared to resistance welding. However, incorporating an internal shaft design significantly

enhances the compressive strength. The compressive strength values for the single-piece, adhesive-bonded, and resistance-welded 14-inch beams are 5,162 N, 4,790 N, and 3,550 N, respectively. The bonding strength efficiencies for the adhesive-bonded and resistance-welded beams are 92.79% and 68.77%, respectively (bonding strength efficiency = the strength of a bonded cord/the strength of a single continuous cord).

Regarding compressive stiffness, the single-piece, adhesive-bonded, and resistance-welded 14-inch beams demonstrate 1,523 N/mm, 1,064 N/mm, and 1,076 N/mm, respectively. A detailed comparison and summary of these three types of beams can be found in **Table 3**. The lateral displacements were measured using DIC experiments, and the critical compressive buckling loads were subsequently determined.

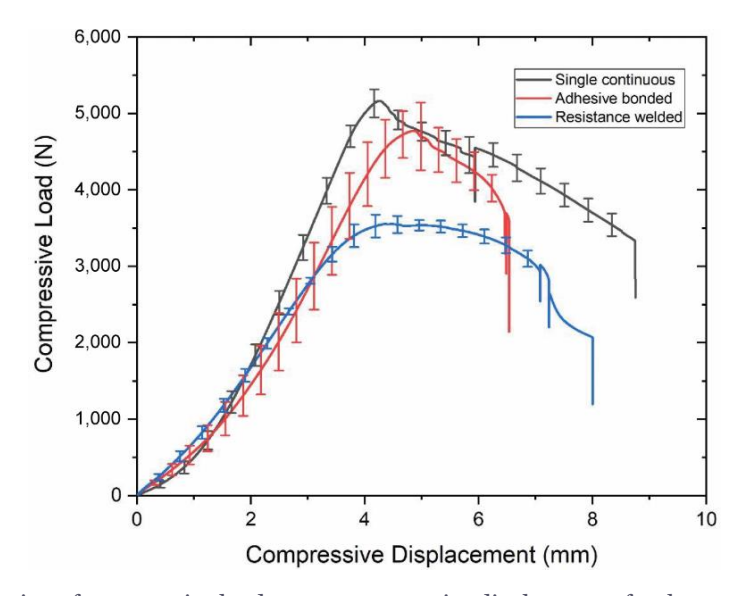


**Figure 6 •** Graphical representation of compressive load versus compressive displacement for three types of beams under compression tests. Each beam is constructed by connecting three identical cords, each set of three beams utilizing different cord types. The solid lines are an average of the three tests on identical chords. The error bars represent the deviation from the averaged curves.

Table 3 • The compressive buckling tests on the three types of 14-inch beams

Sample (14-inch beam)	k <sub>c</sub> (N/mm)	P <sub>max</sub> (N)	σ <sub>y</sub> (MPa)	$A_{\rm c}$ (mm²)	<i>I</i> <sub>c</sub> (mm <sup>4</sup> )	<i>P</i> <sub>cr</sub> (N)	$E_{ m long}$ / $E_{ m tran}$	<i>U</i> <sub>c</sub> (N·mm)
Single piece	1,523.6	5,162.0	7.46	649.9	7,381.7	3,290.3	1.61	28,550.1
Resistance welded	1,076.9	3,550.4	5.12	649.9	7,381.7	1,917.6	1.14	19,609.6
Adhesive bonded	1,064.3	4,790.2	7.91	649.9	7,381.7	2,986.4	1.13	17,865.2

Note:  $k_{\rm c}$  is the compressive stiffness,  $P_{\rm max}$  is the maximum compressive load,  $\sigma_{\rm y}$  is the compressive at the yield point,  $A_{\rm c}$  is the cross-sectional area,  $I_{\rm c}$  is the second moment of inertia in the cross-sectional area,  $P_{\rm cr}$  is the critical compressive buckling load,  $E_{\rm long}/E_{\rm tran}$  is the ratio of stiffness between the longitudinal and transverse directions, and  $U_{\rm c}$  is the energy absorption until the fracture occurs.

The first buckling modes for each of the three types of the 14-inch beam are depicted in **Figures** 7–9. During the experiments, three critical stages were identified, starting from the onset of

compressive buckling and continuing until fracture initiation. A global buckling mode was observed in all three types of beams, suggesting that the stiffness of the fusion-joined region is comparable to that of the 3D-printed sections of the beams.

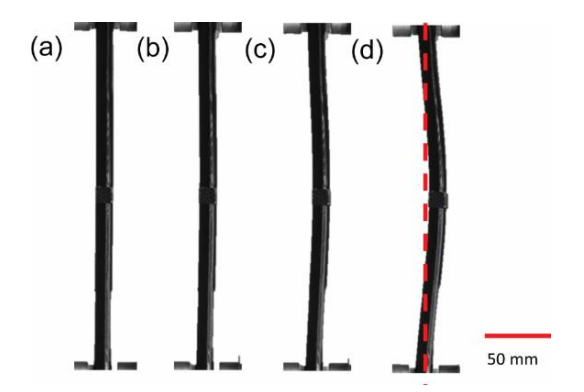


**Figure 7 •** Illustration of the first buckling mode of the single-piece 14-inch beam under uniaxial compression load. (a) Deformation at 100 s (compressive displacement: 2.5 mm), (b) deformation at 125 s (compressive displacement: 3.1 mm), (c) deformation at 150 s (compressive displacement: 3.7 mm), and (d) deformation at 200 s (compressive displacement: 5 mm). Note: Stage (a) represents the critical stage where compressive buckling initiates, and stage (d) marks fracture initiation.

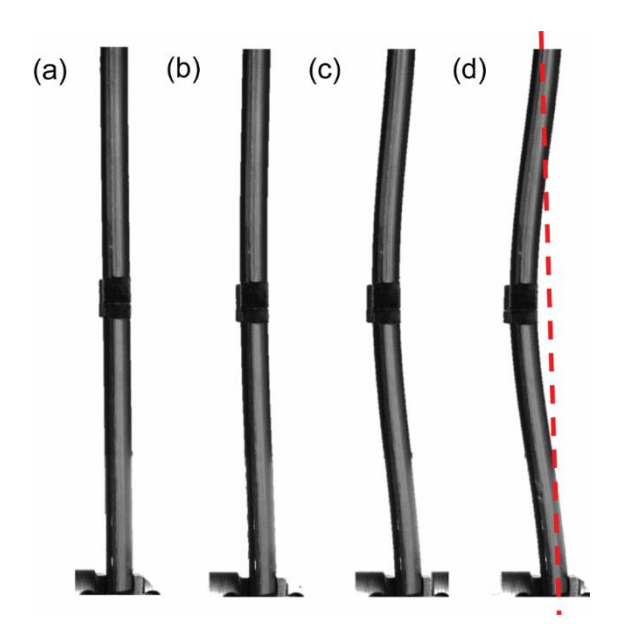


**Figure 8** • Display of the first buckling mode of the adhesive-bonded 14-inch beam subjected to uniaxial compression load. The stages of deformation are captured at different time intervals: (a) deformation at 100 s (compressive displacement: 2.5 mm), (b) deformation at 125 s (compressive displacement: 3.1 mm), (c) deformation at 150 s (compressive displacement: 3.7 mm), and (d) deformation at 200 s (compressive displacement: 5 mm).

The first buckling modes for each type of 14-inch beam were recorded using a sequence of images at a frame rate of 1 fps. Notably, in the case of the single-piece 14-inch beam, no significant lateral displacement was observed within the first 25 s (compressive displacement: 0.6 mm), in contrast to the other two types of beams. This suggests that the single-piece beam can withstand a high load (ultimate compressive stress) for a considerable time (~100 s) or compressive displacement (2.5 mm) before any visible buckling shape becomes apparent.

In comparison, the resistance-welded and adhesive-bonded 14-inch beams exhibited visible buckling shapes after approximately 50 s or 0.8 mm in compressive displacement. Interestingly, the resistance-welded 6-inch chord showed more significant lateral displacement than the adhesive-bonded beam. Initially, the post-buckling behavior of the adhesive-bonded and resistance-welded 7-inch chords appeared similar. However, as time progressed, the resistance-welded 14-inch beam underwent more severe buckling and ultimately failed earlier than its counterparts. Despite these differences, all three types of beams demonstrated a global buckling mode.

The first principal strain distributions of the adhesive-bonded and resistance-welded 14-inch beams are shown in **Figure 10**. Compared to the single 3D-printed 14-inch beams, the first principal strain distribution of resistance-welded 14-inch beams mitigated from the outer edge into the inner bonding line owing to the residual stress induced in this region.

Analysis of **Figure 10** reveals distinct differences in the first principal strain patterns between the adhesive-bonded and resistance-welded 14-inch beams. In the adhesive-bonded beam, the highest strain is concentrated at the edge, gradually diminishing along the bonding line and extending into the outer surrounding substrates. Conversely, in the resistance-welded beam, the highest strain is centrally located near the edge and diffuses more evenly into the surrounding substrates under

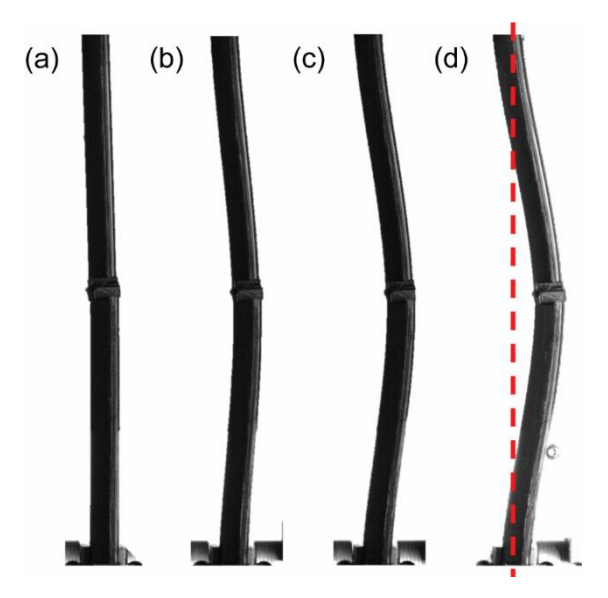


**Figure 9 •** Overview of the first buckling mode of the resistance-welded 14-inch beam under uniaxial compression load. Each critical stages are captured at different time intervals: (a) deformation at 75 s (compressive displacement: 1.9 mm), (b) deformation at 125 s (compressive displacement: 3.1 mm), (c) deformation at 150 s (compressive displacement: 3.7 mm), and (d) deformation at 200 s (compressive displacement: 5 mm).

tension. This pattern suggests that, in cases where the bonding strength is uniformly distributed along the bonding line, the edge is typically the first site for crack initiation due to the maximum surface tension in that region. However, for the resistance-welded 14-inch beam, variations in bonding strength along the bonding line are observed, likely due to nonuniform impregnation during the welding process. Notably, the first principal strain in the resistance-welded beam is higher than in the adhesive-bonded beam, implying that the resistance-welded bonding area can absorb more energy. Therefore, while the resistance welding process demonstrates the potential for achieving higher bonding quality, addressing the issue of nonuniform bonding is crucial for optimizing its effectiveness.

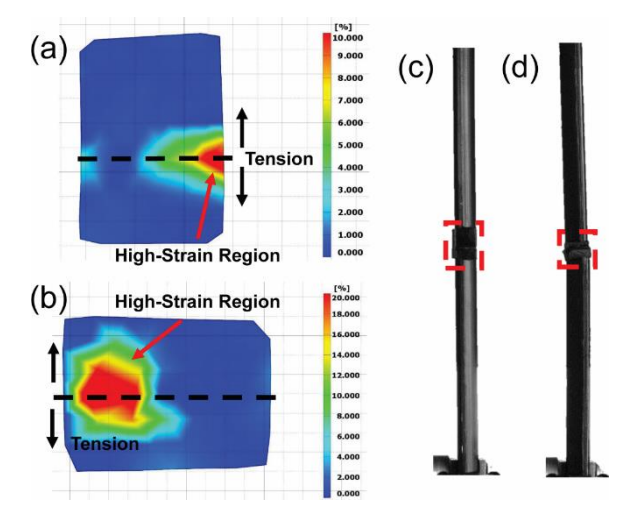


**Figure 10 •** Visualization of the first principal strain distribution as determined by DIC in the bonding region of the 14-inch beam at the initial fracture stage. The figure includes: (a) the adhesive-bonded beam, (b) the resistance-welded beam, and close-up views of the region of interest for (c) the adhesive-bonded beam and (d) the resistance-welded beam.

**Figure 11** displays images depicting the failure modes of the three types of 14-inch beams. The fractures in these beams primarily propagated along the edge line of the rectangular polymer block. This pattern of failure is attributed to the sharp geometric transition from the airfoil span to the rectangular polymer block, which likely acted as a stress concentrator.

The initiation of failure in all three types of 14-inch beams is predominantly observed in the middle and bottom sections of the rectangular box area. This pattern can be attributed to the uneven outer geometric transition from the airfoil to the sharp edges of the rectangular box. Stress analysis at these sharp edges revealed a stress ratio of 1:2, underscoring the importance of smooth outer geometry in airfoil structure design. An uneven surface can significantly reduce the load capacity in localized areas.

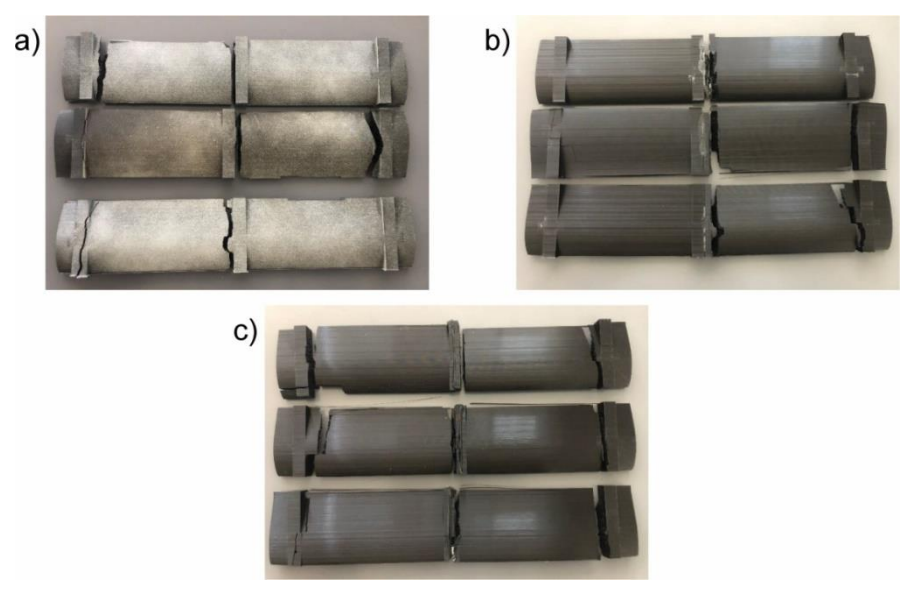


**Figure 11 •** Images of the fractured 14-inch beams. The images include (a) a 3D-printed single-piece 14-inch beam, (b) a 14-inch beam assembled by adhesive bonding two 7-inch chords, and (c) a 14-inch beam created by resistance welding two 7-inch chords.

While the rectangular box design in our experiments created a uniform region of interest for compressive buckling experiments, it is not an ideal structural design in practical applications. Additionally, in some adhesive-bonded and resistance-welded 6-inch chords, cracks were observed to initiate on the inner side of the bonding line, subsequently spreading to the outer 3D-printed substrate. This highlights that the bonding area remains vulnerable in the structure and warrants further reinforcement.

In all three beam types, the propagation and rapid breakage of cracks are influenced by the nature of the PLA material and the low adhesion strength between adjacent deposited layers. Therefore, improving layer adhesion strength is critical for enhancing the structural integrity of these beams.

## **3.2.** Hybrid FEM compression modeling of 14-inch beams formed by connecting the three types of 7-inch chords

**Figure 12** presents the compressive stress versus compressive displacement curves for the three types of 14-inch beams. The primary objective of these curves is to validate the accuracy of the FEM simulations. The results demonstrate that both the CZM and the hybrid CZM approaches successfully achieved high accuracy in the simulations.

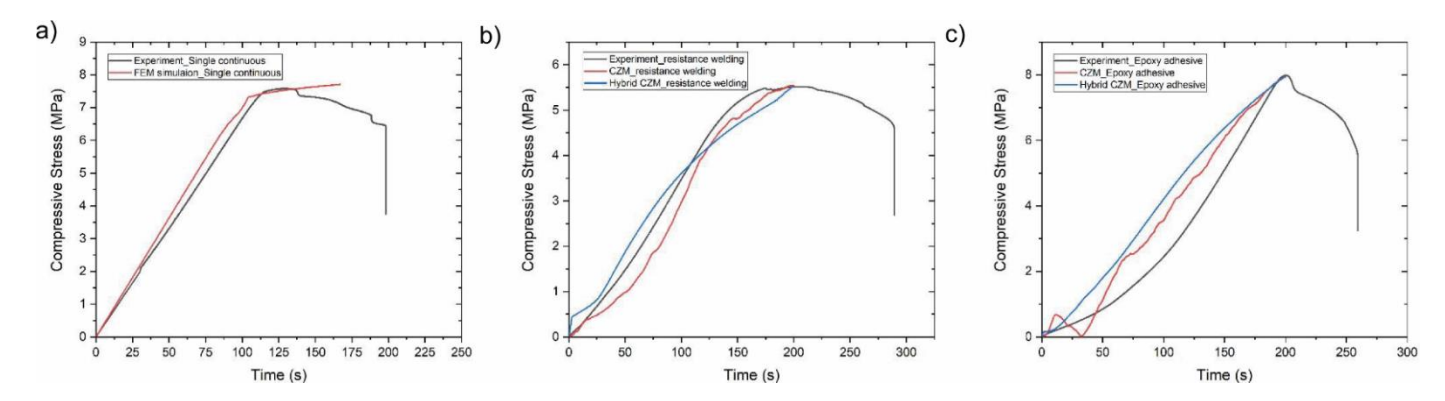


**Figure 12 •** Compressive stress versus compressive displacement curves of the 14-inch beams under experimental and FEM simulation configurations. The images include (a) single piece, (b) resistance welded, and (c) adhesive bonded.

In **Figure 12**, it is evident that all FEM simulations were carried out until the ultimate compressive strength was reached. For the single-piece 14-inch beam, including plasticity in the model

enhanced its alignment with the experimental curve, a step that was not deemed necessary for the other two beam types. Notably,

both the CZM and the hybrid CZM approaches exhibited good agreement with the experimental curves.

However, the limitations of the CZM approach in terms of numerical accuracy become apparent in Figure 12c. As depicted in Figure 12b, when the stiffness of the bonding interphase is sufficiently high (CZM: cohesive stiffness at 1.83 GPa/mm), the CZM approach can replicate a similar stress versus time response as observed in the experimental results. However, as illustrated in **Figure 11c**, when the stiffness of the bonding interphase is slightly lower, as in the case of resistance welding (CZM: cohesive stiffness at 1.12 GPa/mm), the initial phase of the FEM computation exhibits instability (unstable duration from o to 70 s, equivalent to 0-1.75 mm compressive displacement) before stabilizing. This instability, particularly evident in the elastic region, can significantly affect the critical buckling load and the numerical computation, especially when sensitive to the cohesive parameters related to interphase thickness ( $t \approx 10^{-4}$  mm). A lower interphase thickness increases the sensitivity of the computation results and prolongs the time required to achieve an accurate outcome.

Therefore, considering the limitations observed in the CZM approach, it may not be the most suitable solution for predicting the mechanical behavior of fusion-joined engineering structures due to these sensitivities and instabilities.

**Figure 13** illustrates the influence of layer thickness and the ratio of solid to cohesive elements on the compressive strength of the fusion-joined beam. It is crucial to accurately represent the bonding line thickness and the solid–cohesive element ratio in the model, as these factors significantly influence the compressive strength of the 3D-printed structure. The analysis shows that a thinner bonding line with more solid elements increases compressive strength in the fusion-joined beam under similar boundary conditions. Based on the observation of **Figure 13**, the suggested interphase thickness and solid–cohesive element ratio are 10–100  $\mu$ m and 50–75%, respectively. This visualization aids in making the bonding line region in the model more representative of real-world scenarios, thereby enhancing the accuracy and reliability of the simulations.

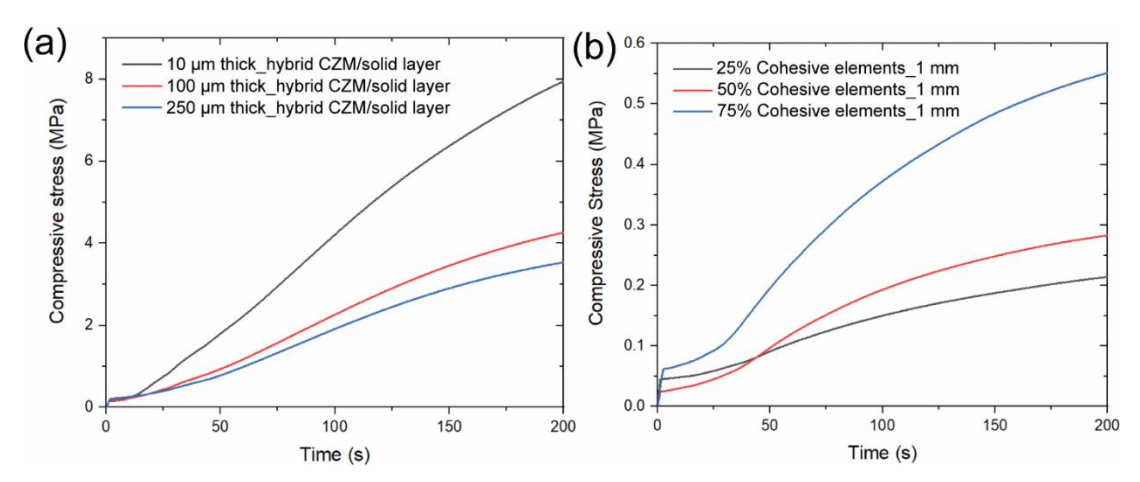


**Figure 13 •** Graphs showing compressive stress versus compressive displacement for the adhesive-bonded 14-inch beam. The figure highlights (a) the effect of interphase thickness, with a distribution of 23% solid elements and 77% cohesive elements; and (b) the effect of varying the ratio of solid to cohesive elements.

The initial setting for the interphase thickness was based on the average thickness of the sample ( $t \approx 1 \, \mathrm{mm}$ ). However, as observed in **Figure 13b**, the ultimate compressive stress of the adhesive-bonded 14-inch beam did not align closely with the actual experimental value, approximately 8 MPa. It was found that simply increasing the interphase stiffness is not an effective strategy, as it results in a marginal increase in strength efficiency and can lead to unrealistically high stress concentrations, thereby underestimating the critical buckling load.

As suggested by the findings in **Figure 13b**, a more practical approach involves maintaining the interphase stiffness within a reasonable range (1–5 GPa [56]) while reducing the interphase thickness. This adjustment better replicates the ultimate compressive stress over compressive displacement. The figure also indicates that higher compressive stress is observed when a lower proportion of solid elements is used in the bonding interphase, attributable to the reduction in cross-sectional area under a similar compressive load. However, the relationship between actual compressive stress and the proportion of solid elements is not linear. The compressive load is borne not only by the solid elements but also by the cohesive elements. While cohesive elements contribute to the load, solid elements play a more

significant role, especially in determining the critical buckling load in the hybrid element CZM.

**Table 4** illustrates the influence of cohesive stiffness on the lateral displacement of the fusion-joined beam. In the context of compressive buckling observation, it is not sufficient to merely match the compressive stress of the fusion-joined beam as a function of time for structural validation. Equally important is the assessment of the beam's lateral displacement over time. This aspect of the analysis is particularly sensitive to the cohesive stiffness of the elements within the bonding line, underscoring the need for an accurate representation of these parameters in the model.

The cohesive stiffness of the bonding interphase plays a significant role in determining the lateral displacement of the 14-inch beam during a uniaxial compression test. It is necessary to use a sufficiently thin interphase in the bonding region to accentuate the role of cohesive stiffness. Despite this, the amount of lateral displacement is primarily influenced by the properties of the solid elements, which typically possess higher stiffness than the cohesive elements. Consequently, fine-tuning the cohesive parameters remains essential to optimize the compressive buckling behavior of the 14-inch beams.

**Table 4** • The lateral displacement versus cohesive stiffness for beams under compression

Sample (14-inch beam)	Cohesive stiffness (MPa)	Lateral displacement (mm)
	0.1	10.18
Adhesive bonded	1	9.85
	10	9.78
	0.1	12.69
Resistance welded	1	12.90
	10	12.75

This table presents data for beams formed by adhesive bonding or resistance welding three 14-inch-long segments.

**Figure 14** shows both the DIC results and the FEM simulation plots for the adhesive-bonded and resistance-welded 14-inch beams. This figure includes plots of the first-order principal strain distribution for the adhesive-bonded beams and the lateral displacement of the resistance-welded beams, as derived from

the model. These plots are then benchmarked against the corresponding DIC images. The comparison of these results indicates a strong correlation between the FEM simulations and the DIC images, demonstrating the accuracy of the FEM in replicating the strains and displacement patterns.

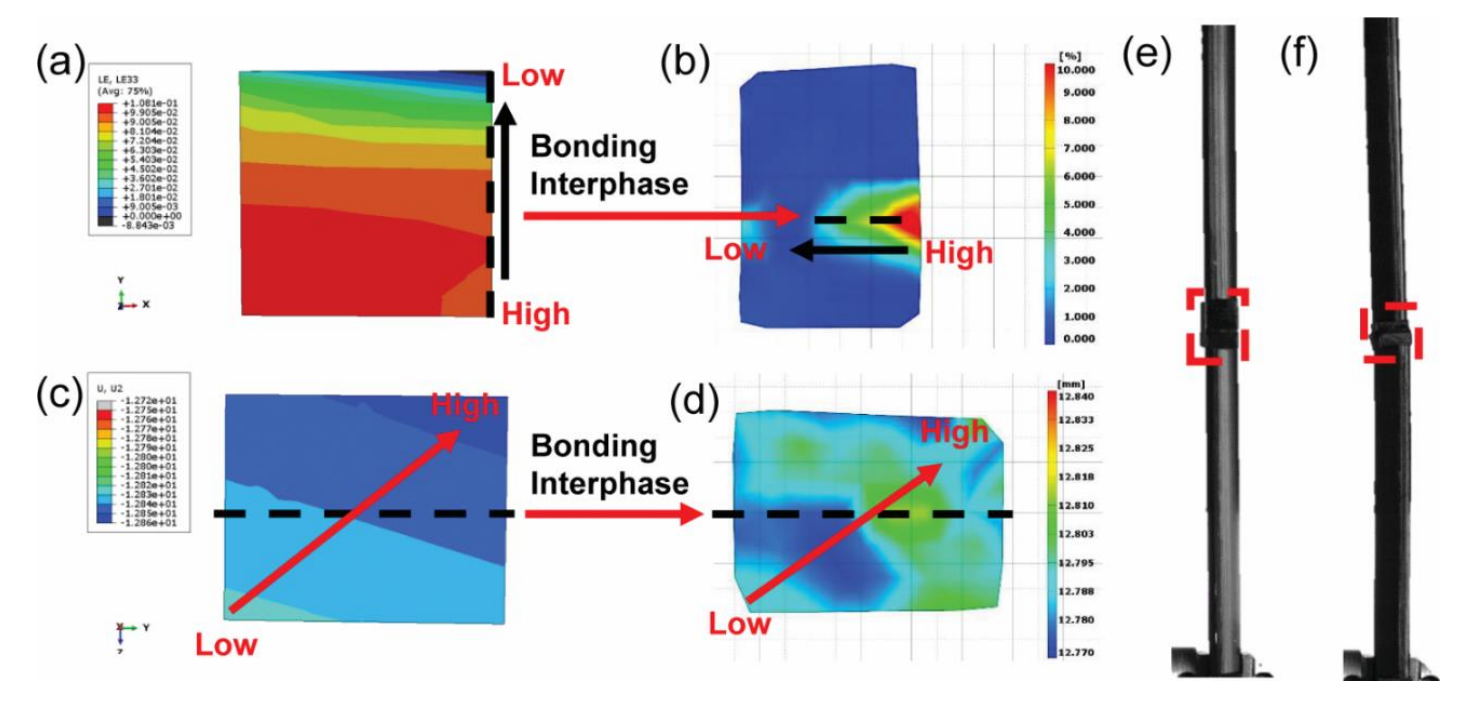


Figure 14 • Comparison of strain distribution and lateral displacement at the fracture initiation stage for adhesive-bonded and resistance-welded 14-inch beams, as determined by DIC results and FEM simulation plots. The figure includes (a) longitudinal strain plot on the bonding interphase for the adhesive-bonded beam, as modeled by the hybrid element CZM approach; (b) first principal strain plot on the bonding interphase for the adhesive-bonded beam, as captured by DIC; (c) lateral displacement plot on the bonding area for the resistance-welded beam, as modeled by the hybrid element CZM approach; (d) lateral displacement plot on the bonding area for the resistance-welded beam, as captured by DIC; (e) detailed view of the region of interest for the adhesive-bonded 14-inch beam; and (f) detailed view of the region of interest for the resistance-welded 14-inch beam.

The hybrid element CZM plots are benchmarked against DIC images to enhance the numerical accuracy concerning the solid-cohesive element ratio. In these plots, the cohesive element represents the softening region within the interphase, a characteristic that can be adjusted by modifying the number of elements involved. This benchmarking process focuses on the fracture initiation stage to ensure precision.

Maintaining an appropriate proportion of cohesive elements in the interphase is critical for accurately capturing the softening behavior at the desired loading stage. It also helps minimize computational costs, which can escalate with excessive cohesive elements [40]. Both the adhesive-bonded and resistancewelded 14-inch beams demonstrate strong concordance with the experimental data and numerical results, validating the effectiveness of the applied modeling approach.

**Figure 15** shows the distribution of longitudinal strain and lateral displacement on the bonding interphase for the adhesive-bonded and resistance-welded 14-inch beams. The numerical values depicted in these models strongly agree with the results obtained from compressive buckling experiments. This correlation underlines the accuracy of the modeling in replicating the physical behaviors observed in the experiments.

After adjusting the ratio of solid to cohesive elements based on the softening area observed during the critical buckling state of the two types of 14-inch beams, the longitudinal strain and lateral displacement at the bonding interphase were compared between the hybrid CZM approach and DIC measurements. In this numerical comparison, the adhesive-bonded 14-inch beam correlated more closely with the DIC results than the resistance-welded beam. This discrepancy is attributed to the nonuniform

stiffness distribution along the bonding region of the resistance-welded beam. The hybrid CZM approach operates under the assumption of uniform stiffness in the interphase region, a simplification that may not entirely reflect realistic conditions.

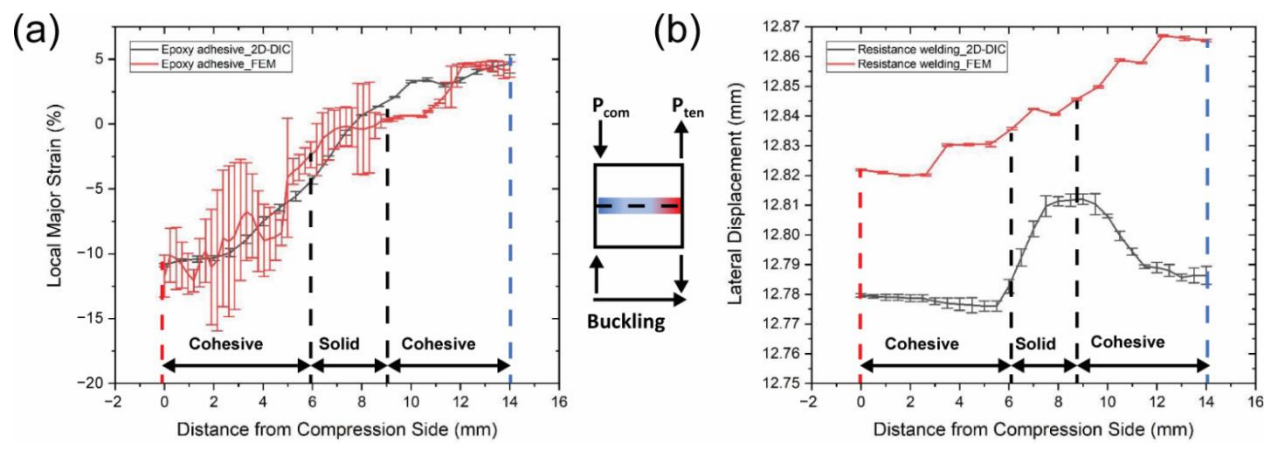


**Figure 15 •** FEM results of the principal strain and lateral displacement distribution in the bonding region of 14-inch beams. The figure (a) illustrates the longitudinal strain distribution at the fracture initiation state in the bonding interphase of an adhesive-bonded 14-inch beam and (b) shows the lateral displacement distribution at the fracture initiation state in the bonding interphase for a resistance-welded 6-inch chord. Note: The red dashed line and red zone indicate areas under compression, while the blue dashed line and blue zone represent areas under tension.

As the primary focus of this study is to determine the critical buckling load using hybrid CZM modeling, no disparities in lateral displacement or first principal strain were observed under DIC measurements at the critical buckling state (lateral displacement = 1 mm). Consequently, uniform stiffness was presumed for both the adhesive-bonded and resistance-welded 14-inch beams in the hybrid CZM models. However, it is worth noting that the hybrid CZM approach can model discontinuous interphase stiffness by modifying local element stiffness, particularly when considering fracture behavior.

**Figure 16** displays the energy absorption in the bonding region as a function of lateral displacement for both adhesive-bonded and resistance-welded 14-inch beams. In the case of the adhesive-bonded 14-inch beam, the stable energy absorption observed in the bonding line can be attributed to the mechanical interlocking between the male shaft and the female locket. Furthermore, the high level of crystallization in the PLA and the compressive residual stress between the PLA and metallic fibers in the bonding line is crucial for maintaining stable energy absorption during post-buckling scenarios.

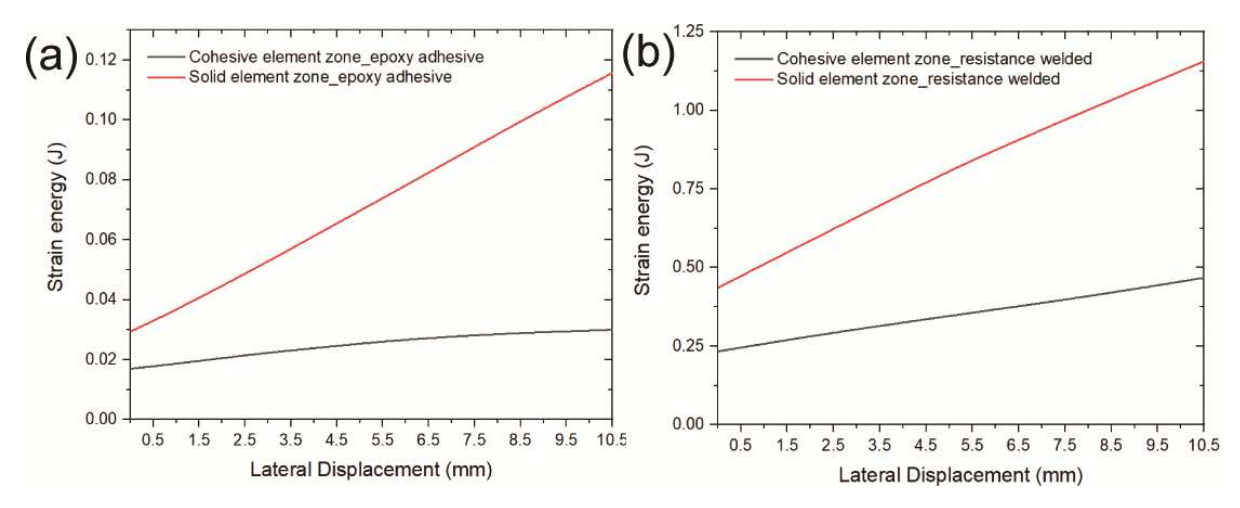


**Figure 16 •** Graph showing energy absorption in the bonding region as a function of lateral displacement for 14-inch beams. The figure includes two parts: (a) representing the adhesive-bonded beam and (b) depicting the resistance-welded beam.

During the compressive buckling test, the force exerted on the bonding interphase of both resistance-welded and adhesive-bonded 14-inch beams was predominantly compressive before the onset of buckling. It was observed that the cohesive elements in these beams could store more potential energy than solid elements until compressive deformations reached 1.25 mm and 1.75 mm, respectively, for the resistance-welded and adhesive-bonded beams. However, once buckling was initiated, the loading on the bonding interphase changed: it was no longer purely

compressive, as the shear load was induced due to lateral displacement, transforming the compressive load into a bending load.

In the post-buckling phase, solid elements bear a substantially higher bending load than cohesive elements. Therefore, incorporating solid elements into the bonding interphase is crucial for accurately modeling compressive buckling performance, such as in the computation of critical buckling loads. While increasing

the shear stiffness of cohesive elements is theoretically possible for modeling compressive buckling, this approach can lead to computational convergence challenges. Employing solid elements, in contrast, can significantly reduce computational costs while maintaining high accuracy.

When comparing adhesive-bonded and resistance-welded 14-inch beams, it was noted that the strain energy on the bonding interphase of the resistance-welded beams was considerably higher than that of the adhesive-bonded beams, attributable to thicker bonding interphase and greater interphase stiffness. At the critical buckling stage, the strain energies for the resistance-

welded and adhesive-bonded beams were measured at 1.09 J and 2.48 J, respectively. Furthermore, at the fracture initiation stage, the strain energies were recorded at 10.44 J for the resistance-welded beam and 11.31 J for the adhesive-bonded beam.

**Table 5** summarizes various parameters, including uniaxial compressive stress, compressive strain, lateral displacement, energy absorption, and peak first principal strain on the bonding interphase of the 14-inch beams. Through the combined use of DIC and uniaxial compressive buckling tests, the accuracy of the FEM was thoroughly validated. This table serves as a reference for comparing the experimental data with FEM predictions, thereby confirming the reliability of the simulation results.

**Table 5** • Detailed metrics at the fracture initiation stage (marking the end of the post-buckling stage) for 14-inch beams, including uniaxial compressive stress ( $\sigma_{\rm uni}$ ), compressive strain ( $\varepsilon_{\rm uni}$ ), lateral displacement ( $d_{\rm lat}$ ), energy absorption ( $U_{\rm total}$ ), and peak first principal strain ( $\varepsilon_{\rm lat}$ ) specifically measured at the bonding interphase of the 14-inch beams

Sample (14-inch beam)	σ <sub>uni</sub> (MPa)	ε <sub>uni</sub> (mm/mm)	d <sub>lat_FEM</sub> (mm)	d <sub>lat_DIC</sub> (mm)	ε <sub>lat_FEM</sub> (mm/mm)	ε <sub>lat_DIC</sub> (mm/mm)	$egin{aligned} oldsymbol{U_{total}} \ ig( \mathbf{J}  /  \mathbf{m}^3 ig) \end{aligned}$
Single piece	7.94	0.0139	6.75	6.92	0.0293	_	-
Resistance welded	5.46	0.0139	13.09	13.04	0.2007	0.2065	5.33 × 10 <sup>5</sup>
Adhesive bonded	7.36	0.0139	9.79	9.82	0.1081	0.1154	1.37 × 10 <sup>6</sup>

## 3.3. Critical buckling load and buckling modes of the 14-inch beams

**Figures 17–19** illustrate the relationship between the critical buckling load and the slenderness ratio for 14-inch beams across multiple buckling modes (modes 1–3). The use of the hybrid element CZM approach in these figures demonstrates high accuracy for all three slenderness ratios across the three buckling modes. When comparing the simulation results with experimental data, it becomes apparent that both Euler's and Johnson's methods have limitations in accurately predicting the buckling load for fusion-joined structures.

In the first flexural buckling mode context, the hybrid CZM approach demonstrates a good correlation with the results of compressive buckling tests, especially for beams with a slenderness ratio of 6. However, the Euler and Johnson formulas tend to underestimate the critical buckling loads by approximately 33% and 34% for the resistance-welded beams and about 25% for the adhesive-bonded 14-inch beams, respectively.

When considering beams with higher slenderness ratios (specifically 12 and 18 in the simulation, compared to the critical slenderness ratio, in this case, of 13.2 in the experiment), the predicted compressive buckling loads from the hybrid element CZM approach and Euler's formula show closer agreement. This indicates that while Euler's formula may have limitations at lower slenderness ratios, its accuracy improves for beams with higher slenderness ratios.

Regarding the second flexural buckling mode, the Euler formula's estimates for critical buckling loads exceed those of the hybrid element CZM approach by 48% and 31% for the resistance-welded and adhesive-bonded 14-inch beams, respectively, at a slenderness ratio of 6. When considering higher slenderness ratios (12 and 18), the discrepancy widens: the Euler

formula predicts compressive buckling loads that are 68% and 78% higher than the hybrid CZM approach for the resistance-welded 6-inch chords and 50% and 59% higher for the adhesive-bonded 6-inch chords, respectively.

As for the Johnson formula, its predictions for the resistance-welded 14-inch beams are 53% higher at a slenderness ratio of 12 but 19% lower at a slenderness ratio of 6. For the adhesive-bonded 14-inch beams, the Johnson formula estimates are 46% higher at a slenderness ratio of 12 and 35% lower at a slenderness ratio of 6. These findings highlight the varying degrees of accuracy between these formulas and the hybrid element CZM approach, particularly across different slenderness ratios and beam types.

In the third flexural buckling mode context, the Euler formula significantly overestimates the critical buckling loads compared to the hybrid element CZM approach. For resistance-welded and adhesive-bonded 14-inch beams at a slenderness ratio of 6, the Euler formula's estimates are higher by 230% and 105%, respectively. With higher slenderness ratios of 12 and 18, the discrepancy remains notable: the Euler formula predicts compressive buckling loads 98% and 156% higher than the hybrid CZM approach for resistance-welded beams and 74% and 83% higher for adhesive-bonded beams, respectively.

Concerning the Johnson formula, its predictions for the resistance-welded 14-inch beams are 63% higher at a slenderness ratio of 12 and 88% higher at 18 but 12% lower at 6. For adhesive-bonded beams, the Johnson formula estimates the compressive buckling load to be 33% higher at a slenderness ratio of 12, 78% higher at 18, but 50% lower at 6. These results highlight the significant variation in accuracy between these traditional formulas and the hybrid element CZM approach, especially as the slenderness ratio changes.

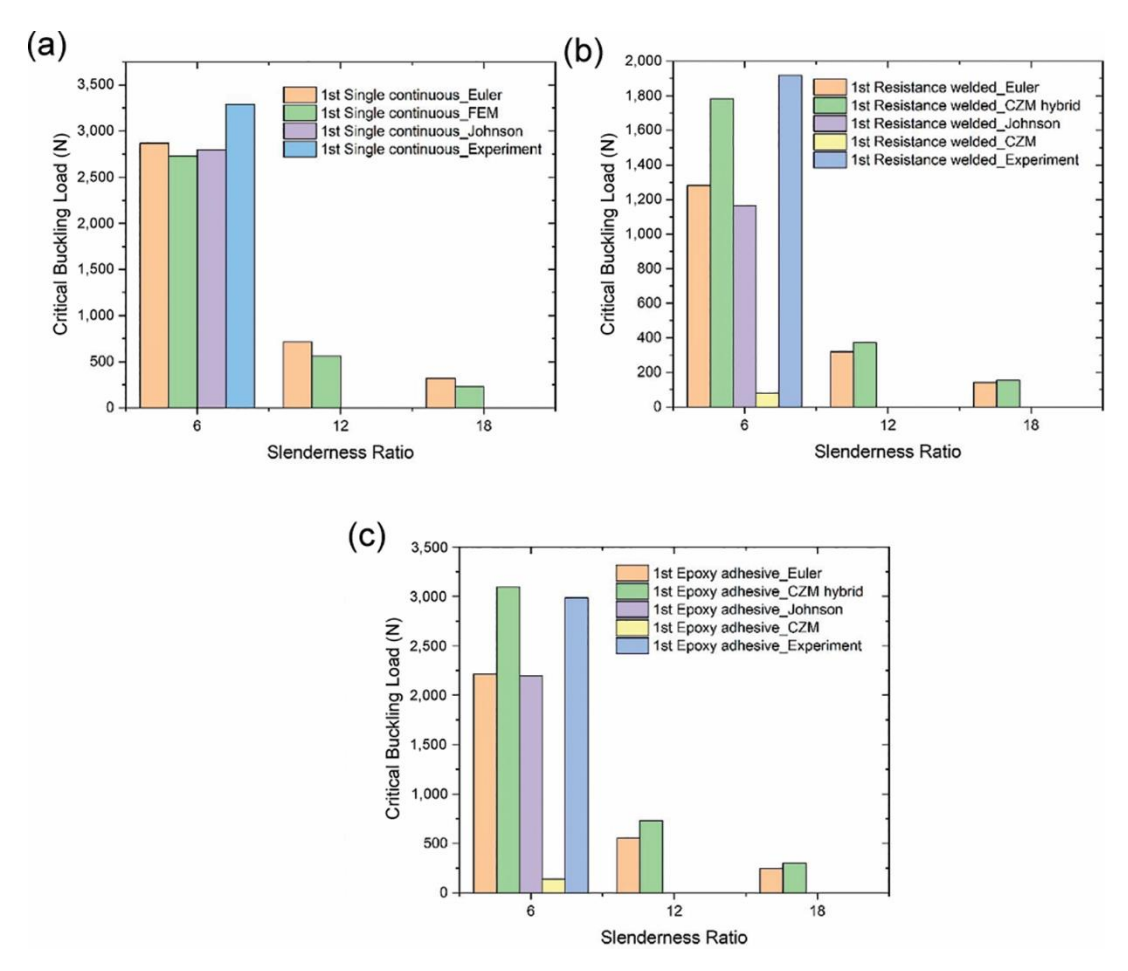


**Figure 17 •** Graph showing the relationship between critical buckling load and beam slenderness ratio for 14-inch beams under mode one flexural buckling: (a) the single-piece beam, (b) the resistance-welded beam, and (c) the adhesive-bonded beam.

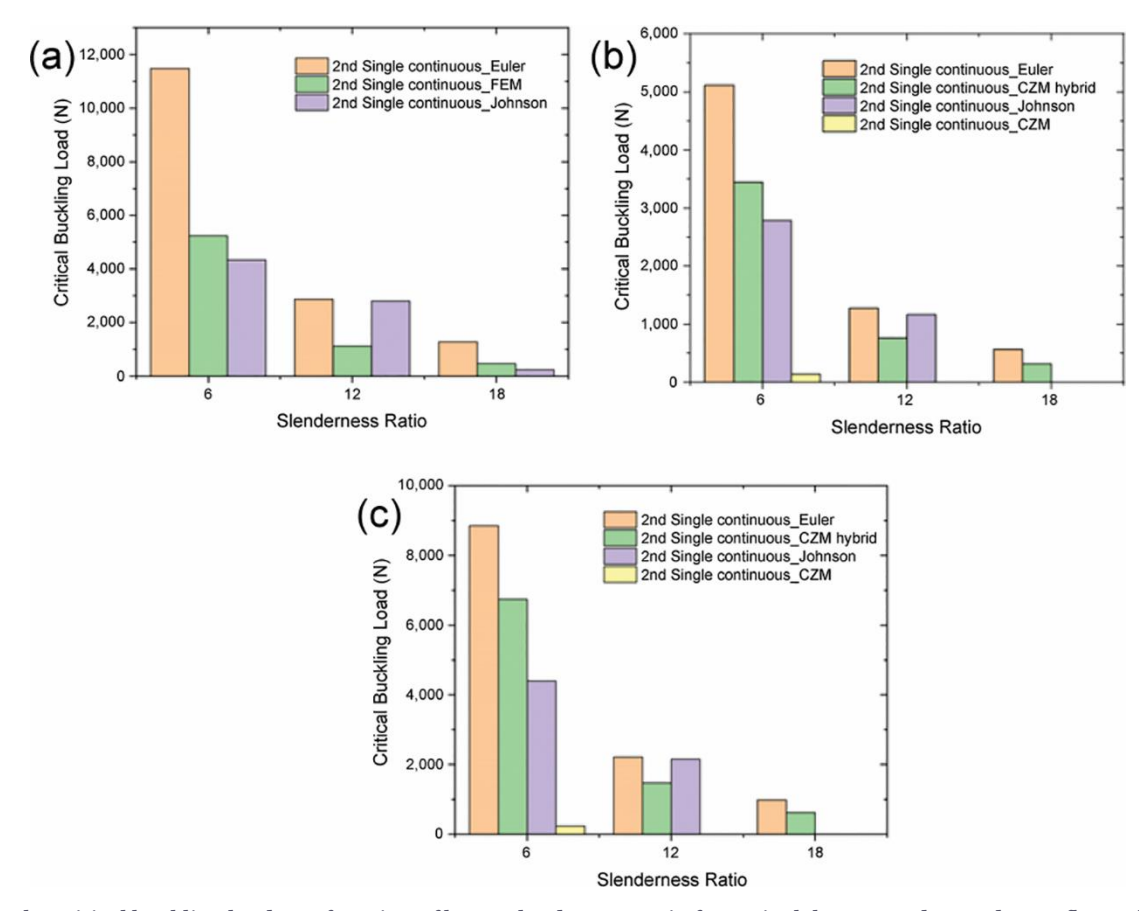


**Figure 18 •** The critical buckling load as a function of beam slenderness ratio for 14-inch beams under mode two flexural buckling: (a) the single-piece beam, (b) the resistance-welded beam, and (c) the adhesive-bonded beam.

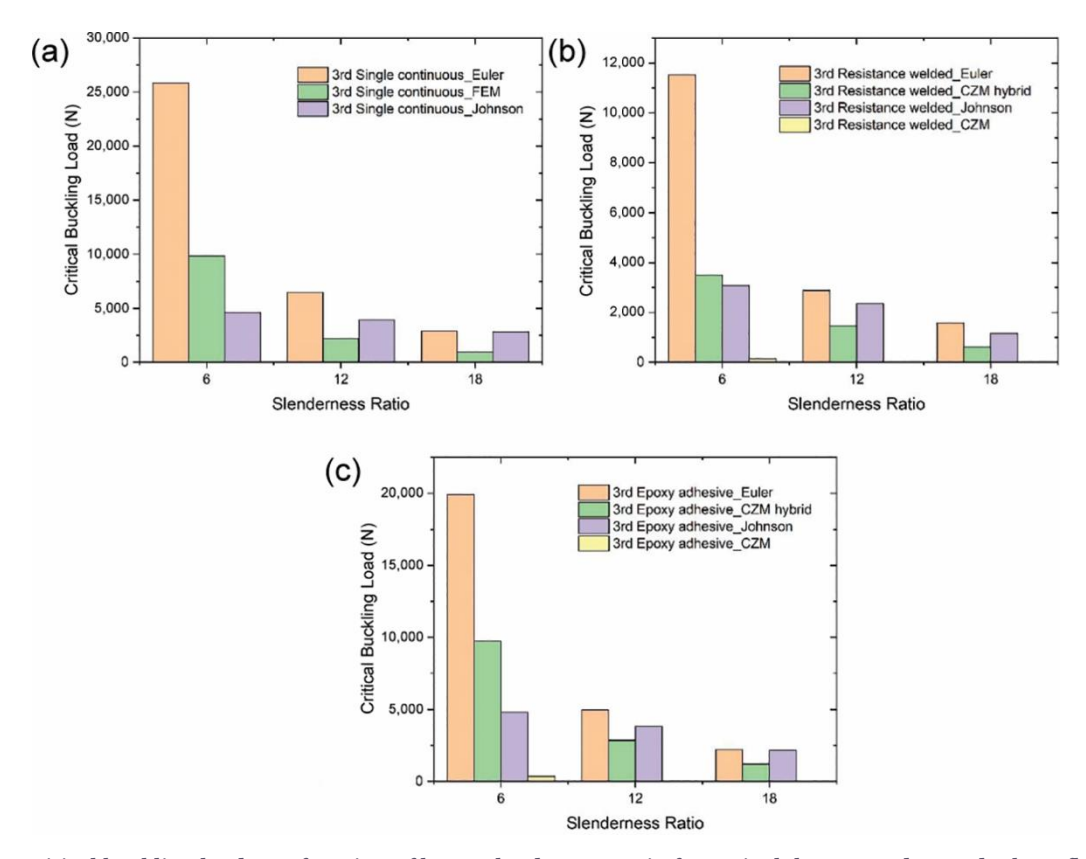


**Figure 19 •** The critical buckling load as a function of beam slenderness ratio for 14-inch beams under mode three flexural buckling: (a) the single-piece beam, (b) the resistance-welded beam, and (c) the adhesive-bonded beam.

Overall, the Euler formula accurately predicts the first flexural buckling mode for resistance-welded and adhesive-bonded 14-inch beams, mainly when the slenderness ratio is high (greater than 12). On the other hand, the Johnson formula tends to be more accurate for the second and third flexural buckling modes in resistance-welded and adhesive-bonded 14-inch beams, significantly when the slenderness ratio ranges between 6 and 12. This differentiation in accuracy underscores the importance of selecting the appropriate formula based on the specific buckling mode and the slenderness ratio of the beams under consideration.

**Figures 20–22** show the flexural buckling modes of single-piece, resistance-welded, and adhesive-bonded 14-inch beams. These figures reveal that the stress distribution and buckling modes exhibit notable similarities across all three beam types. This consistency in behavior provides valuable insights into the structural characteristics and performance under buckling conditions for each type of beam.

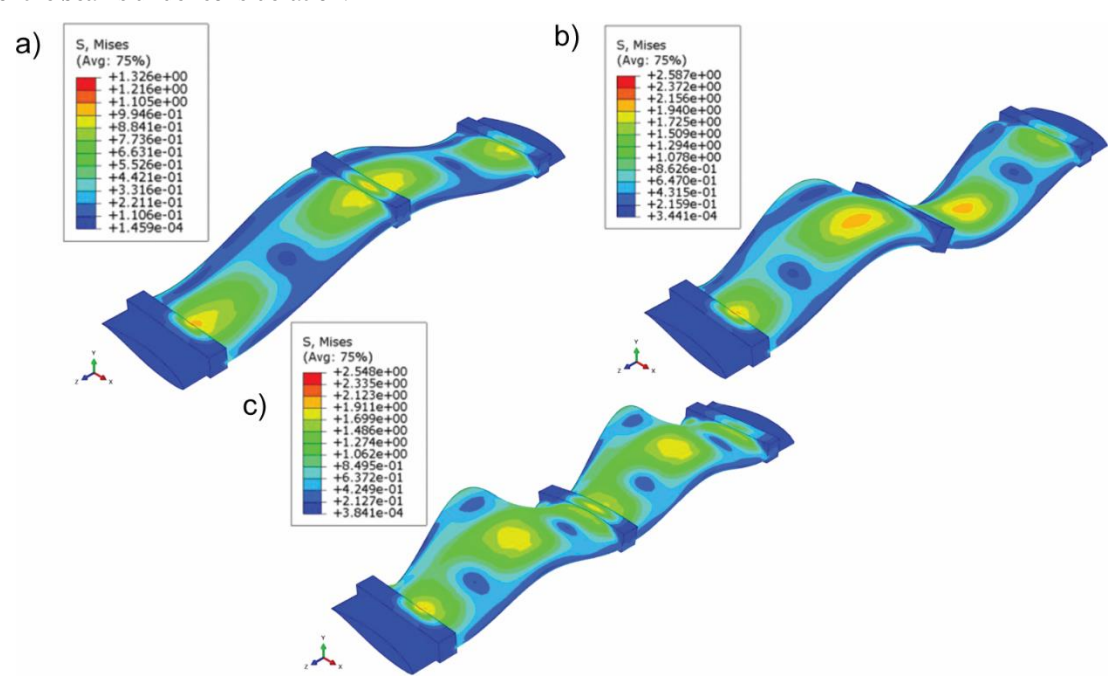


**Figure 20 •** Visualization of flexural buckling modes in single-piece 14-inch beams. The figure illustrates (a) the first flexural buckling mode, (b) the second flexural buckling mode, and (c) the third flexural buckling mode. Note: The deformation in these images is upscaled by a factor of 35.56 for a more precise visualization.

The observed buckling modes of the resistance-welded and adhesive-bonded 14-inch beams closely resemble those of the single-piece 14-inch beam. This similarity suggests that the bonding in the interphase does not significantly affect the buckling modes, thereby validating the efficacy of resistance welding and adhesive bonding as reliable methods for fusion joining thermoplastic polymers. However, it is noteworthy that the single-piece 14-inch beam facilitates a smoother stress flow along its entire span.

In contrast, areas of high stress concentration are noted at the buckling peaks and along the rectangular edges in the resistance-welded and adhesive-bonded beams, attributable to lower bonding strength at the interphase. This observation underscores the need to enhance the bonding strength in resistance-welded and adhesive-bonded 14-inch beams to achieve a more uniform stress distribution throughout the structure. The numerical values of critical buckling loads of 14-inch beams are listed in **Tables 6–9**.

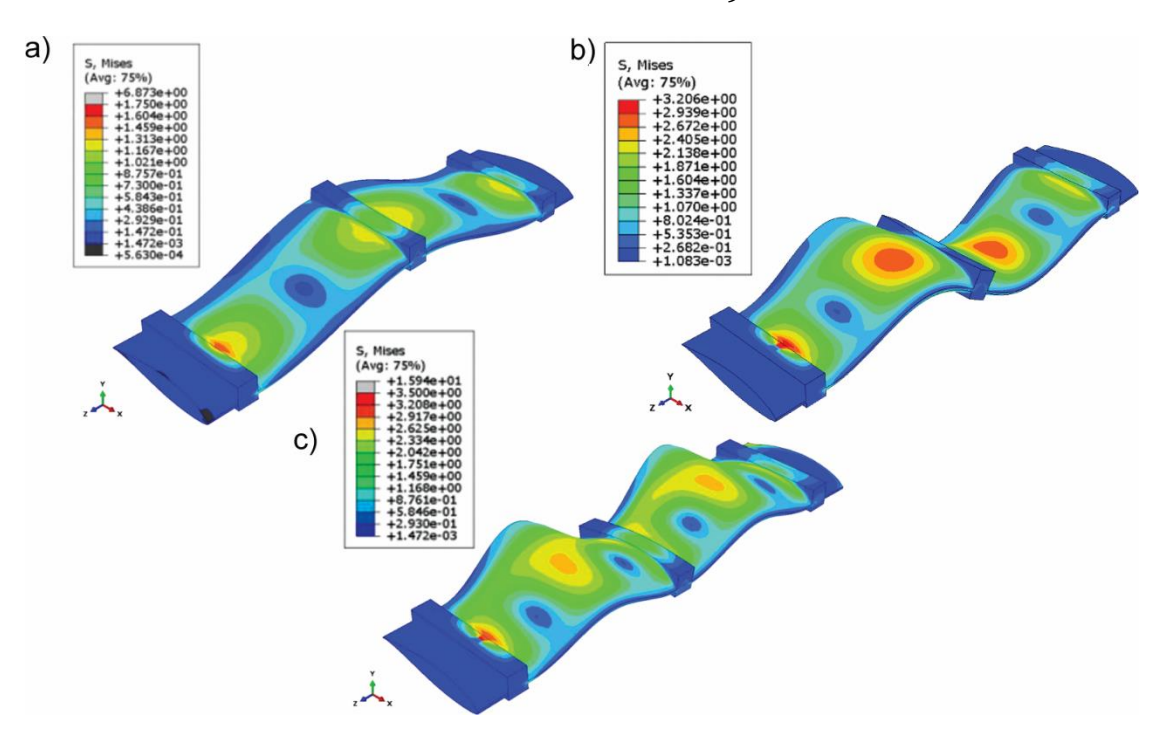


**Figure 21 •** Visualization of flexural buckling modal shapes for an adhesive-bonded 14-inch beam. The figure includes (a) the first flexural buckling mode, (b) the second flexural buckling mode, and (c) the third flexural buckling mode. Note: The deformation in these images is upscaled by a factor of 29.91 to facilitate clearer visualization.

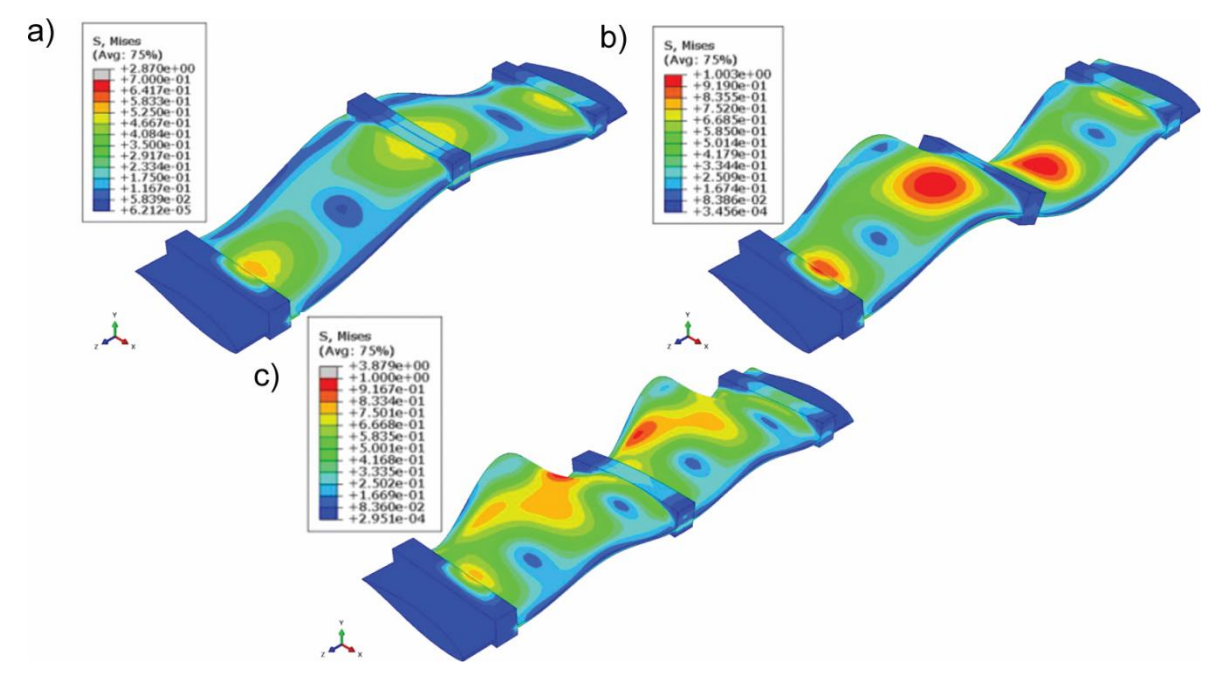


**Figure 22** • Illustration of flexural buckling modal shapes in resistance-welded 14-inch beams. This figure demonstrates (a) the first flexural buckling mode, (b) the second flexural buckling mode, and (c) the third flexural buckling mode. Note: The deformation depicted in these images is upscaled by a factor of 29.34 for an enhanced visualization.

Table 6 • Critical buckling loads of 14-inch beams under different buckling modes

Sample (14-inch beam)	Approach	Buckling load (N) (mode 1)	Buckling load (N) (mode 2)	Buckling load (N) (mode 3)
Single piece	Euler	2,868.51	11,473.85	25,816.16
	Johnson	2,799.74	4,336.63	4,621.24
	FEM	2,730.80	5,230.40	9,841.50
Resistance welded	Euler	1,280.84	5,123.37	11,527.58
	Johnson	1,166.24	2,787.52	3,087.76
	FEM-CZM	81.57	137.74	210.62
	FEM-CZM hybrid	1,782.01	3,452.75	6,040.10
Adhesive bonded	Euler	2,212.66	8,850.62	19,913.90
	Johnson	2,154.71	4,394.74	4,809.56
	FEM-CZM	140.92	237.94	363.84
	FEM-CZM hybrid	3,095.97	6,743.65	9,714.75

Note: The mode indicates the order of the buckling shape of the 14-inch beam.

 $\textbf{Table 7} \bullet \textbf{Compilation of critical buckling loads for 14-inch beams under various slenderness ratios in the first flexural buckling mode$ 

Sample (14-inch beam)	Approach	Buckling load (N) (SR: 6)	Buckling load (N) (SR: 12)	Buckling load (N) (SR: 18)
Single piece	Euler	2,868.51	717.12	318.72
	Johnson	2,799.74	-	-
	FEM	2,730.80	558.93	232.44
Resistance welded	Euler	1,280.84	320.21	142.32
	Johnson	1,166.24	-	-
	FEM-CZM	81.57	-	-
	FEM-CZM hybrid	1,782.01	372.26	156.18
Adhesive bonded	Euler	2,212.66	553.16	245.85
	Johnson	2,198.12	-	_
	FEM-CZM	140.92	-	-
	FEM-CZM hybrid	3,095.97	730.33	304.50

Note: SR indicates the slenderness ratio of the 14-inch beam. This table provides a detailed comparison of how critical buckling loads vary with changes in the slenderness ratio for this specific buckling mode.

 $\textbf{Table 8} \bullet \textbf{Summary of critical buckling loads for 14-inch beams across various slenderness ratios in the second flexural buckling mode$ 

Sample (14-inch beam)	Approach	Buckling load (N) (SR: 6)	Buckling load (N) (SR: 12)	Buckling load (N) (SR: 18)
Single piece	Euler	11,473.84	2,868.46	1,274.87
	Johnson	4,336.63	2,799.73	238.25
	FEM	5,230.40	1,119.67	469.41
Resistance welded	Euler	5,123.37	1,280.84	569.26
	Johnson	2,787.52	1,166.24	-
	FEM-CZM	137.74	_	-
	FEM-CZM hybrid	3,452.75	760.55	319.96
Adhesive bonded	Euler	8,850.62	2,212.7	983.40
	Johnson	4,394.74	2,154.7	-
	FEM-CZM	237.94	_	-
	FEM-CZM hybrid	6,743.65	1,471.97	618.28

This table presents a detailed analysis of how critical buckling loads are influenced by different slenderness ratios specific to the second mode of flexural buckling.

**Table 9 •** Detailed overview of critical buckling loads for 14-inch beams at various slenderness ratios in the third flexural buckling mode

Sample (14-inch beam)	Approach	Buckling load (N) (SR: 6)	Buckling load (N) (SR: 12)	Buckling load (N) (SR: 18)
Single piece	Euler	25,816	6,454	2,869
	Johnson	4,621	3,938	2,799
	FEM	9,841.50	2,204.44	925.00
Resistance welded	Euler	11,528	2,882	1,584.09
	Johnson	3,088	2,367	1,166
	FEM-CZM	140.92	-	-
	FEM-CZM hybrid	3,495.97	1,455.65	619.86
Adhesive bonded	Euler	19,914	4,979	2,213
	Johnson	4,810	3,814	2,155
	FEM-CZM	363.84	-	-
	FEM-CZM hybrid	9,714.75	2,864.57	1,210.67

This table provides an in-depth comparison, illustrating how critical buckling loads vary with different slenderness ratios, specifically in the context of the third mode of flexural buckling.

The hybrid element CZM method has successfully predicted the compressive buckling loads of fusion-joined 14-inch beams across three different slenderness ratios. While the Euler and

Johnson formulas remain valid and valuable under certain conditions, the versatility of the hybrid element CZM method stands out. It offers the capability to predict compressive buckling loads

and modes for fusion-joined beams with a wide range of slenderness ratios, making it a more flexible and broadly applicable tool in structural analysis.

#### 4. Conclusions

Thin-walled lattice structures with an airfoil cross section using 14-inch beams 3D printed with FDM were successfully fabricated, which were then fusion joined using epoxy adhesive and resistance welding. The critical buckling loads of single-piece, adhesive-bonded, and resistance-welded 14-inch beams were determined using the Euler analytical formula, Johnson analytical formula, DIC experiments, and a hybrid element CZM numerical approach. Buckling modes were also analyzed using nonlinear buckling analysis (Abaqus–Riks method).

Two modeling methodologies were implemented: the first method employed CZM to replicate the buckling performance of fusion-joined beams, while the second utilized solid—cohesive hybrid elements for a more visual representation of buckling performance. The results indicate that the latter approach (solid—cohesive hybrid elements) outperforms the former (cohesive zone modeling) in capturing the critical buckling loads and modes. This novel strategy for nonlinear buckling modeling represents a significant advancement over traditional CZM, particularly in the context of fusion-joined additive-manufactured structures.

While the Euler and Johnson formulas can accurately predict the critical compressive buckling loads of fusion-joined structures with high (>12) and intermediate (6–12) slenderness ratios due to the minimal effect of heterogeneous interphase bonding, their accuracy is limited to the first flexural buckling mode. These formulas falter in accurately determining the critical loads for lower slenderness ratios (<6) and higher-order buckling modes, where the sensitivity of numerical accuracy becomes a significant factor due to variables, such as yield stress, heterogeneity, bonding stiffness and strength, and slenderness ratio.

Consequently, the hybrid element CZM approach emerges as a robust method for predicting linear and post-buckling performance in structures with varying slenderness ratios and higher-order buckling modes. This work underscores the importance of considering heterogeneous behavior in the interphase bonding region between joining segments to comprehensively understand the buckling behavior of fusion-joined, additive-manufactured slender structures.

#### Acknowledgments

We wish to express gratefulness to Louis A. Beecherl Jr. Chair for supporting H.L.

#### **Funding**

We gratefully acknowledge the support from the National Science Foundation (NSF) under Grant Numbers 2219347 and 1726435, from the NSF WindStar I/UCRC Center under Grant Numbers IIP-1362033 and IIP-1916776, and from the Department of Energy (DOE) under Grant Numbers DE-NA0003962 and DE-NA-0003525.

#### **Author contributions**

Conceptualization, D.C., D.T.G. and H.L.; methodology, D.C.; software, D.C.; validation, D.C., D.T.G. and H.L.; formal analysis, D.C.; investigation, D.C.; resources, D.C.; data curation, D.C.; writing—original draft preparation, D.C.; writing—review and editing, D.C., D.T.G. and H.L.; visualization, D.C.; supervision, D.T.G. and H.L.; project administration, D.T.G. and H.L.; funding acquisition, D.T.G. and H.L. All authors have read and agreed to the published version of the manuscript.

#### Conflict of interest

The authors declare no conflict of interest.

#### Data availability statement

Data supporting these findings are available within the article, at https://doi.org/10.20935/AcadMatSci7281, or upon request.

#### Institutional review board statement

Not applicable.

#### Informed consent statement

Not applicable.

#### Sample availability

The authors declare no physical samples were used in the study.

#### Additional information

Received: 2024-03-21 Accepted: 2024-07-31 Published: 2024-08-22

Academia Materials Science papers should be cited as Academia Materials Science 2024, ISSN 2997-2027, https://doi.org/10.20935/AcadMatSci7281. The journal's official abbreviation is Acad. Mat. Sci.

#### Publisher's note

Academia.edu Journals stays neutral with regard to jurisdictional claims in published maps and institutional affiliations. All claims expressed in this article are solely those of the authors and do not necessarily represent those of their affiliated organizations, or those of the publisher, the editors and the reviewers. Any product that may be evaluated in this article, or claim that may be made by its manufacturer, is not guaranteed or endorsed by the publisher.

#### Copyright

© 2024 copyright by the authors. This article is an open access article distributed under the terms and conditions of the Creative Commons Attribution (CC BY) license (https://creativecommons.org/licenses/by/4.0/).

#### References

- Drumheller DP, D'Antonio GC, Chapman BA, Allison CP, Pierrakos O. Design of a micro-wind turbine for implementation in low wind speed environments. 2015 Systems and Information Engineering Design Symposium; 2015 Apr 24. Charlottesville (VA): IEEE; 2015 p. 125–30. doi: 10. 1109/SIEDS.2015.7116959
- 2. Davis MS, Madani MR. 3D-printing of functional small-scale wind turbine. 2018 6th International Renewable and Sustainable Energy Conference (IRSEC); 2018 Dec 5–8. Rabat: IEEE; 2018.
- 3. Madara SR. Review of recent development in 3-D printing of turbine blades. Eur J Adv Eng Technol. 2017;4(7):497–509.
- 4. Bassett K, Carriveau R, Ting DSK. 3D printed wind turbines part 1: design considerations and rapid manufacture potential. Sustain Energy Technol Assess. 2015;11:186–93. doi: 10.1016/j.seta.2015.01.002
- 5. Freere P, Sacher M, Derricott J, Hanson B. A Low cost wind turbine and blade performance. Wind Eng. 2010;34(3):289. doi: 10.1260/0309-524X.34.3.289
- 6. Hirahara H, Hossain MZ, Kawahashi M, Nonomura Y. Testing basic performance of a very small wind turbine designed for multi-purposes. Renew Energy. 2005;30(8): 1279–97. doi: 10.1016/j.renene.2004.10.009
- 7. Matsumiya H, Ito R, Kawakami M, Matsushita D, Iida M, Arakawa C. Field operation and track tests of 1-kW small wind turbine under high wind conditions. J Sol Energy Eng. 2010;132(1):0110021–8. doi: 10.1115/1.4000330
- 8. Energy Saver. Installing and maintaining a small wind electric system. [cited 2024 Jan]. Available from: https://www.energy.gov/energysaver/installing-and-maintaining-small-wind-electric-system
- 9. Kaminski M, Loth E, Griffith DT, Qin C. Ground testing of a 1% gravo-aeroelastically scaled additively-manufactured wind turbine blade with bio-inspired structural design. Renew Energy. 2020;148:639–50. doi: 10.1016/j.renene. 2019.10.152
- 10. Tummala A, Velamati RK, Sinha DK, Indraja V, Krishna VH. A review on small scale wind turbines. Renew Sustain Energy Rev. 2016;56:1351–71. doi: 10.1016/j.rser.2015.12.027
- Mishnaevsky L. Repair of wind turbine blades: review of methods and related computational mechanics problems. Renew Energy. 2019;140:828-39. doi: 10.1016/j.renene. 2019.03.113
- 12. Stephenson S. Wind blade repair: planning, safety, flexibility. [cited 2021 Jun 1]. Available from: https://www.compositesworld.com/columns/wind-blade-repair-planning-safety-flexibility(2)
- 13. Cripps D. The future of blade repair. Reinf Plast. 2011; 55(1):28–32. doi: 10.1016/S0034-3617(11)70034-0
- 14. Wang X, Jiang M, Zhou Z, Gou J, Hui D. 3D printing of polymer matrix composites: a review and prospective. Compos B Eng. 2017;110:442–58. doi: 10.1016/j.compositesb. 2016.11.034

- 15. Tay YWD, Panda B, Paul SC, Noor Mohamed NA, Tan MJ, Leong KF. 3D printing trends in building and construction industry: a review. Virtual Phys Prototy. 2017;12(3):261–76. doi: 10.1080/17452759.2017.1326724
- Zadi-Maad A, Rohib R, Irawan A. Additive manufacturing for steels: a review. In: IOP Conference Series: Materials Science and Engineering. Vol. 285. Jakarta: Institute of Physics Publishing; 2018. doi:10.1088/1757-899X/285/1/ 012028
- 17. Poole S, Phillips R. Rapid prototyping of small wind turbine blades using additive manufacturing. Proceedings of the 2015 Pattern Recognition Association of South Africa and Robotics and Mechatronics International Conference; 2015 Nov 26–27. Port Elizabeth: IEEE; 2015. p. 189–94. doi: 10.1109/RoboMech.2015.7359521
- 18. Cao D, Malakooti S, Kulkarni VN, Ren Y, Liu Y, Nie X, et al. The effect of resin uptake on the flexural properties of compression molded sandwich composites. Wind Energy. 2022;25:71–93. doi: 10.1002/we.2661
- 19. Li L, Tirado A, Nlebedim IC, Rios O, Post B, Kunc V, et al. Big area additive manufacturing of high performance bonded NdFeB magnets. Sci Rep. 2016;6(1):1–7. doi: 10. 1038/srep36212
- 20. Duty CE, Kunc V, Compton B, Post B, Erdman D, Smith R, et al. Structure and mechanical behavior of Big Area Additive Manufacturing (BAAM) materials. Rapid Prototyp. 2017; 23(1):181–9. doi: 10.1108/RPJ-12-2015-0183
- 21. Strong AB. High performance & engineering thermoplastic composites. Lancaster (PA): Taylor & Francis; 1993.
- 22. Schwartz MM. Joining of composite-matrix materials. Materials Park (OH): ASM International; 1994.
- 23. Yousefpour A, Hojjati M, Immarigeon JP. Fusion bonding/welding of thermoplastic composites. J Thermoplast Compos Mater. 2004;17(4):303-41. doi: 10.1177/0892705704045187
- 24. Grimm R. Welding processes for plastics. Adv Mater Process. 1995;147:27–30.
- 25. Murray RE, Roadman J, Beach R. Fusion joining of thermoplastic composite wind turbine blades: lap-shear bond characterization. Renew Energy. 2019;140:501–12. doi: 10.1016/j.renene.2019.03.085
- 26. Ageorges C, Ye L, Hou M. Advances in fusion bonding techniques for joining thermoplastic matrix composites: a review. Compos Part A Appl Sci Manuf. 2001;32(6):839–57. doi: 10.1016/S1359-835X(00)00166-4
- 27. Stavrov D, Bersee HEN. Resistance welding of thermoplastic composites-an overview. Compos Part A Appl Sci Manuf. 2005;36(1):39–54. doi: 10.1016/j.compositesa.2004.06.030
- 28. Benatar A, Gutowski TG. Review of methods for fusion bonding thermoplastic composites. SAMPE J. 1987;23:120–31.
- Rider AN, Wang CH, Cao J. Internal resistance heating for homogeneous curing of adhesively bonded repairs. Int J Adhes Adhes. 2011;31(3):168–76. doi: 10.1016/j.ijadhadh. 2011.01.001

- 30. Davies P, Cantwell WJ, Jar PY, Bourban PE, Zysman V, Kausch HH. Joining and repair of a carbon fibre-reinforced thermoplastic. Composites. 1991;22(6):425–31. doi: 10.10 16/0010-4361(91)90199-Q
- 31. Dubé M, Hubert P, Yousefpour A, Denault J. Resistance welding of thermoplastic composites skin/stringer joints. Compos Part A Appl Sci Manuf. 2007;38(12):2541–52. doi: 10.1016/J.COMPOSITESA.2007.07.014
- 32. Panneerselvam K, Aravindan S, Noorul Haq A. Study on resistance welding of glass fiber reinforced thermoplastic composites. Mater Des. 2012;41:453-9. doi: 10.1016/J.MATDES.2012.05.025
- 33. Don RC, Gillespie JW, Lambing CLT. Experimental characterization of processing-performance relationships of resistance welded graphite/polyetheretherketone composite joints. Polym Eng Sci. 1992;32(9):620–31. doi: 10.1002/PEN.760320908
- 34. Ageorges C, Ye L, Hou M. Experimental investigation of the resistance welding for thermoplastic-matrix composites. Part I: Heating element and heat transfer. Compos Sci Technol. 2000;60(7):1027–39. doi: 10.1016/S0266-3538 (00)00005-1
- 35. Zhang YX, Yang CH. Recent developments in finite element analysis for laminated composite plates. Compos Struct. 2009; 88(1):147–57. doi: 10.1016/J.COMPSTRUCT.2008.02.014
- 36. Ferreira PS, Virtuoso FBE. Semi-analytical models for the post-buckling analysis and ultimate strength prediction of isotropic and orthotropic plates under uniaxial compression with the unloaded edges free from stresses. Thin Wall Struct. 2014;82:82–94. doi: 10.1016/J.TWS.2014.04.003
- 37. Feng DC, Wu JY. Phase-field regularized cohesive zone model (CZM) and size effect of concrete. Eng Fract Mech. 2018; 197:66–79. doi: 10.1016/J.ENGFRACMECH.2018.04.038
- 38. Nguyen VP, Wu JY. Modeling dynamic fracture of solids with a phase-field regularized cohesive zone model. Comput Methods Appl Mech Eng. 2018;340:1000–22. doi: 10.1016/J.CMA.2018.06.015
- 39. Elices M, Guinea GV, Gómez J, Planas J. The cohesive zone model: advantages, limitations and challenges. Eng Fract Mech. 2002;69(2):137–63. doi: 10.1016/S0013-7944(01) 00083-2
- 40. Cao D, Malakooti S, Kulkarni VN, Ren Y, Lu H. Nanoindentation measurement of core–skin interphase viscoelastic properties in a sandwich glass composite. Mech Time Depend Mater. 2020;25:353–63. doi: 10.1007/s11043-020-09448-y
- 41. Shahrubudin N, Lee TC, Ramlan R. An overview on 3D printing technology: technological, materials, and applications. Procedia Manuf. 2019;35:1286–96. doi: 10.1016/j.promfg.2019.06.089
- 42. Caminero MA, Chacón JM, García-Moreno I, Rodríguez GP. Impact damage resistance of 3D printed continuous fibre reinforced thermoplastic composites using fused deposition modelling. Compos B Eng. 2018;148:93–103. doi: 10.1016/j. compositesb.2018.04.054

- 43. McMaster-Carr. High-temperature nickel-chromium wire cloth. [cited 2021 May 3]. Available from: https://www.mcmaster.com/wire-cloth/material~nickel/
- 44. Cao D, Bouzolin D, Lu H, Griffith DT. Bending and shear improvements in 3D-printed core sandwich composites through modification of resin uptake in the skin/core interphase region. Compos B Eng. 2023;29:110912. doi: 10. 1016/J.COMPOSITESB.2023.110912
- 45. Griffith DT, Richards PW. The SNL100-03 blade: design studies with flatback airfoils for the Sandia 100-Meter Blade; 2014 [cited 2024 Jan]. Available from: https://energy.sandia.gov/wp-content/uploads/dlm\_uploads/1418129.pdf
- 46. Griffith DT, Ashwill TD. The Sandia 100-meter all-glass baseline wind turbine blade: SNL100-00; 2011 [cited 2024 Jan]. p. 1–67. Available from: https://energy.sandia.gov/wp-content/gallery/uploads/SAND2011-3779.pdf
- 47. Griffith DT. The SNL100-02 blade: advanced core material design studies for the Sandia 100- meter blade. 2013. [cited 2024 Jan], Available from: https://energy.sandia.gov/wp-content/gallery/uploads/dlm\_uplo-ads/1310162.pdf
- 48. Griffith DT. The SNL100-01 blade: carbon design studies for the Sandia 100-meter blade; 2013. [cited 2021 May 3]. Available from: https://energy.sandia.gov/wp-content/gallery/uploads/SNL100-01\_NuMAD\_SAND2013-1178.pdf
- 49. Bhat C, Noronha DJ, Saldanha FA. Structural performance evaluation of segmented wind turbine blade through finite element simulation. Int J Mech Mechatron Eng. 2015;9(6): 996–1005.
- 50. Peeters M, Santo G, Degroote J, Van Paepegem W. The concept of segmented wind turbine blades: a review. Energies. 2017;10(8):1–20. doi: 10.3390/en10081112
- 51. Riddell SG, inventor. Joint design for rotor blade segments of a wind turbine. United States patent US7922454B1. 2011 Apr 12.
- 52. B&K Precision. Model 9202, multi-range programmable dc power supplies. [cited 2021 May 4]. Available from: https://www.bkprecision.com/products/power-supplies/9202
- 53. ASTM International. ASTM D6641/D6641M 16e2 standard test method for compressive properties of polymer matrix composite materials using a combined loading compression (CLC) test fixture. 2017. doi: 10.1520/D6641\_D6641M-16
- 54. Stephen T, James G. Theory of elastic stability. 2nd ed. Providence (RI): McGraw-hill International Book Company; 1963.
- 55. Bahabadi HM, Farrokhabadi A, Rahimi GH. Investigation of debonding growth between composite skins and corrugated foam-composite core in sandwich panels under bending loading. Eng Fract Mech. 2020;230:110–23. doi: 10.1016/j.engfracmech.2020.106987
- 56. Hamad K, Kaseem M, Ayyoob M, Joo J, Deri F. Polylactic acid blends: the future of green, light and tough. Prog Polym Sci. 2018;85:83–127. doi: 10.1016/J.PROGPOLYMSCI.2018.07. 001